Driving proteomic imbalance in malignancy provokes proteomic catastrophe and confers tumor suppression

Babul Moni Ram[1], Omprakash Shriwas[1], Meng Xu[1], Kun-Han Chuang[1,2], and Chengkai Dai[1,*]

[1]Mouse Cancer Genetics Program, Center for Cancer Research, National Cancer Institute, Frederick, MD 21702, USA

[2]Present address: School of Basic Medical Sciences, Fujian Medical University, Fuzhou, Fujian 350108, China

*Correspondence: Chengkai.dai@nih.gov

ABSTRACT

Unlike genomic instability, the role of proteomic instability in cancer remains poorly defined. Heat shock factor 1 (HSF1), a master regulator of the proteotoxic stress response, preserves proteome integrity under stress and is increasingly recognized as an oncogenic enabler. In Neurofibromatosis type I (*NF1*)-deficient malignant peripheral nerve sheath tumor (MPNST) cells, *HSF1* loss induces widespread protein polyubiquitination, aggregation, and tumor-suppressive amyloidogenesis, yet is dispensable in non-transformed Schwann cells. Mechanistically, HSF1 protects the mitochondrial chaperone HSP60 from toxic soluble amyloid oligomers. To adapt to compromised protein quality, *HSF1*-deficient MPNST cells activate JNK to repress mTORC1-dependent translation, reducing protein load. Stimulating mTORC1 in these *HSF1*-deficient cells drives catastrophic proteomic imbalance, triggering pronounced cell death, in part through unchecked amyloidogenesis, and suppressing tumor growth *in vivo*. Thus, HSF1 safeguards the cancer proteome, enabling the oncogenic capacity of mTORC1. This proof-of-principle study establishes the induction of proteomic catastrophe as a new paradigm for combating malignancy.

INTRODUCTION

Compared to genomic instability, proteomic instability in cancer is underappreciated. Malignant transformation triggers proteotoxic stress and destabilizes the proteome.[1, 2] Multiple mechanisms, including reactive oxygen species, genetic mutations, and dysregulated protein translation, contribute to increased protein damage, misfolding, and aggregation.[1-3] Notably, amyloidogenesis, a hallmark of neurodegenerative disorders,[4] also occurs in cancer.[5] Unlike neurons, however, cancer cells can contain amyloid formation and mitigate its cytotoxic effects. A key component of this defense is heat shock factor 1 (HSF1), which drives the heat shock response/proteotoxic stress response (HSR/PSR), a potent cytoprotective transcriptional program.[6-8] Consistent with its role in repressing proteomic instability, HSF1 has emerged as a powerful oncogenic enabler independent of driver mutations.[9-15]

In contrast to its dispensability in normal and non-transformed cells, HSF1 is essential in many cancer cell lines,[9,13,16-18] due to elevated intrinsic proteotoxic stress. This dependency, termed "non-oncogene addiction" to HSF1,[2,19] highlights its potential as a therapeutic target.

Neurofibromatosis type 1 (NF1) is a cancer predisposition syndrome affecting approximately 1 in 3000 individuals worldwide.[20] About 30-50% of NF1 patients develop benign plexiform neurofibromas, which can progress into highly aggressive malignant peripheral nerve sheath tumors (MPNSTs) with poor prognosis.[21] The *NF1* gene encodes neurofibromin, a 250-280 kDa RAS GTPase activating protein (GAP) that negatively regulates RAS signaling.[22] Loss of *NF1* in MPNST cells leads to hyperactive RAS/MAPK signaling, which not only promotes cellular growth but also drives constitutive HSF1 activation.[13] Accordingly, HSF1 overexpression and activation

are observed in both experimental MPNST models and primary NF1 tumors.[13] Significantly, *Hsf1* deficiency impaired NF1-associated tumorigenesis in mice, partly through attenuation of oncogenic RAS signaling.[13]

Utilizing the NF1 tumor model system, we herein identify HSF1 as a central regulator that counteracts proteomic instability in cancer. We demonstrate that amyloidogenesis occurs in *NF1*-deficient MPNST cells, driven in part by hyperactive mTORC1 signaling and increased protein translation. Inhibition of HSF1 destabilizes the cancer proteome, leading to widespread protein polyubiquitination, aggregation, and amyloid formation. This proteomic instability, ultimately, causes cytotoxicity. To survive HSF1 inhibition, MPNST cells activate JNK to suppress mTORC1 and reduce protein synthesis. Disruption of this adaptative response via JNK inhibition exacerbates amyloidogenesis and cell death. Similarly, mTORC1 stimulation—via genetic *TSC2* depletion or supplementation with leucine or its analog—synergizes with HSF1 inhibition to induce profound proteomic chaos and widespread non-apoptotic cell death. Notably, blocking amyloidogenesis significantly rescues cell viability. Together, these findings reveal a critical role for HSF1 in antagonizing proteomic instability in cancer cells, representing a general pro-oncogenic mechanism. This work provides proof of principle that inducing proteomic catastrophe may serve as a next-generation anti-cancer therapeutic strategy.

RESULTS

HSF1 counters proteomic instability in *NF1*-deficient MPNST cells

We previously demonstrated that *NF1* loss leads to constitutive HSF1 activation and that *Hsf1* deficiency impairs tumorigenesis in *Nf1*$^{+/-}$; *p53*$^{+/-}$ (NPcis) mice.[13] Consistent with these findings, analysis of human cancers revealed that *NF1* deletion is associated with elevated *HSF1* gene expression (Figure 1A), and *NF1* and *HSF1* expression levels are inversely correlated (Figure S1A). Importantly, among patients with *NF1*-deleted tumors, higher *HSF1* expression correlates with reduced survival (Figure 1B). Together, these data support a pro-oncogenic role for HSF1 in *NF1*-deficient malignancies.

Given the critical role of HSF1 in protein homeostasis, we examined how its depletion impacts the proteome of *NF1*-deficient MPNST cells compared to *NF1*-proficient, non-transformed human Schwann cells (HSCs), both primary and immortalized. HSCs are the presumed cell of origin for MPNSTs.[20,22] In three different MPNST cell lines (90-8TL, S462, and SNF96.2), transient *HSF1* depletion, using two previously validated lentiviral shRNAs,[9,13] led to a marked increase in global protein Lys48-specific polyubiquitination, a molecular mark for proteasomal degradation,[23] in both detergent-soluble and -insoluble fractions (Figures 1C, 1D, S1B, and S1C), indicative of widespread protein misfolding and aggregation. In contrast, no such increase was observed in HSCs (Figures 1C and 1D). These results indicate that HSF1 is specifically required to maintain proteomic stability in malignant Schwann cells.

While most cellular protein aggregates are amorphous, a subset adopts highly ordered β-sheet-rich structures known as amyloids, which are classically associated with neurodegenerative disorders,

116 especially Alzheimer's disease.[24] To determine whether *HSF1* depletion induces amyloidogenesis,
117 we stained cells with Congo red (CR), a widely applied amyloid-binding fluorescent dye.[25]
118 MPNST cells exhibited stronger CR staining than HSCs at baseline (Figure 1E), suggesting higher
119 amyloid burden in malignant cells. Notably, *HSF1* depletion further increased CR staining in
120 MPNST cells but not in HSCs (Figures 1E, 1F, S1D, and S1E). Similar results were obtained using
121 Thioflavin T staining (Figure S1F), another popular amyloid dye.[25] We further validated amyloid
122 accumulation using ELISA with two conformation-specific antibodies (A11 and OC), which
123 recognize soluble amyloid oligomers (AOs) and insoluble amyloid fibrils (AFs), respectively.[26,27]
124 *HSF1* depletion significantly increased both $A11^+$ AOs and OC^+ AFs across all three MPNST cell
125 lines (Figures 1G, 1H, S1G-S1J), whereas no significant changes were detected in HSCs (Figures
126 1I and 1J). Collectively, these findings indicate that HSF1 is essential for maintaining proteome
127 integrity in malignant Schwann cells, particularly by suppressing amyloidogenesis, while being
128 largely dispensable in non-transformed Schwann cells.
129
130 **Unchecked proteomic instability is cytotoxic**
131 It has become evident that HSF1 acts as a generic oncogenic enabler; nevertheless, a universal
132 underlying mechanism has yet to be fully defined.
133
134 A healthy proteome enables the translation of genotypes into phenotypes. Thus, we reasoned that
135 preservation of proteomic stability represents a fundamental pro-oncogenic mechanism of HSF1.
136 To test this, we first determined whether proteomic instability—particularly amyloidogenesis—is
137 causally related to the cytotoxicity induced by *HSF1* depletion in cancer cells. To inhibit amyloid
138 formation, we employed CR, which exerts anti-amyloid effects through its amyloid-binding

activity.[5,28,29] Consistent with the concept of "non-oncogene addiction" in cancer, *HSF1* depletion markedly impaired the viability of MPNST cells. Significantly, CR treatment partially rescued this impaired viability (Figures 2A, S2A, and S2B), indicating that amyloidogenesis contributes to the cytotoxic effects of HSF1 inhibition. In contrast, neither *HSF1* depletion nor CR treatment affected the viability of HSCs (Figure 2B), congruent with their lack of proteomic instability and amyloidogenesis. Together, these findings demonstrate that unchecked proteomic instability—particularly amyloidogenesis—is cytotoxic. Accordingly, HSF1 enables oncogenesis, at least in part, by constraining proteomic instability.

HSF1 neutralizes soluble amyloid oligomers to protect MPNST cells

How does HSF1 counter amyloid toxicity to enable the growth and survival of MPNST cells? In previous research using tissue overgrowth models, we discovered that HSF1, unexpectedly, physically neutralizes soluble AOs, thereby preventing their assault on HSP60.[30] As an essential mitochondrial chaperone, HSP60 safeguards the mitochondrial proteome.[30-32]

We next asked whether this mechanism operates in cancer cells. Co-IP experiments indicated that $A11^{+}$ AOs physically interacted with HSF1, but not major HSPs, in MPNST cells (Figure 2C), consistent with our previous findings.[30] This AO–HSF1 interaction was further validated using an independent technique, *in situ* Proximity Ligation Assay (PLA) (Figures 2D-2F). Significantly, *HSF1* depletion promoted the AO–HSP60 interaction (Figure 2G and 2H). Given that loss of *HSP60* destabilized the mitochondrial proteome,[30,32] this AO–HSP60 interaction signifies the induction of mitochondrial damage and subsequent cytotoxicity. Collectively, our

161 findings reveal that HSF1 protects MPNST cells, at least in part, by neutralizing soluble AOs,
162 thereby preserving the mitochondrial chaperone HSP60 function (Figure 2I).
163
164 **MPNST cells react to HSF1 deficiency by activating JNK to attenuate translation**
165 Given their dependency on HSF1, cancer cells are expected to engage adaptive responses to
166 survive its inhibition. Previously, we uncovered that in *Hsf1*-deficient mice, the stress-responsive
167 JNK kinase becomes constitutively activated, leading to disassembly of mTORC1 through
168 phosphorylation of its core components, RAPTOR and mTOR.[33] This inhibition of mTORC1
169 diminishes protein translation, leading to reduced cell size and whole-body lean mass in *Hsf1*-
170 deficient mice.[33]
171
172 We therefore hypothesized that cancer cells might exploit this same molecular regulation for
173 survival and adaptation. In MPNST cells, *HSF1* knockdown activated JNK, as indicated by
174 increased phosphorylation at T183/Y185. This activation was accompanied by suppression of
175 mTORC1 signaling, evidenced by diminished p70S6K T389 and 4EBP1 S65/T70
176 phosphorylation (Figures 3A, 3B, and S3A-S3D).[34,35] In contrast, *HSF*1 knockdown had minimal
177 effects on JNK and mTORC1 signaling in non-transformed HSCs (Figures 3A and 3B). Detected
178 by PLA, in MPNST cells HSF1 interacted with JNK. Upon *HSF1* depletion, JNK–RAPTOR
179 interactions increased, while mTOR–RAPTOR interactions decreased (Figures 3C-3E). Because
180 the mTOR-RAPTOR interaction is essential for mTORC1 assembly and activity,[36] these findings
181 indicate that JNK senses HSF1 deficiency to repress mTORC1. Notably, this sensing mechanism
182 appears more prominent in malignant cells than in non-transformed counterparts.
183

184 Consistent with mTORC1 inhibition, *HSF1* depletion reduced global protein translation rate in
185 MPNST cells (Figures 3F, S3E, and S3F), as measured by puromycin labeling.[33,37] This
186 regulatory relationship was conserved across diverse human cancer cell lines (Figure 3G).
187 Importantly, treatment with JNK-IN-8, an irreversible JNK inhibitor,[38] largely restored protein
188 translation following *HSF1* depletion and increased basal translation rates (Figures 3F, S3E, and
189 S3F). Consistent with these observations, in human cancers higher *HSF1* expression correlates
190 with lower JNK activation (Figure S3G), which in turn is associated with elevated mTORC1
191 activity, as indicated by increased 4EBP1 Ser65 phosphorylation (Figure S3H). In aggregate, our
192 findings demonstrate that JNK activation mediates mTORC1 inhibition and translational
193 suppression in response to *HSF1* deficiency. Thus, by restraining JNK signaling, HSF1 permits
194 robust protein translation fundamental to malignant growth (Figure 3H).
195
196 **Lowering protein quantity is an adaptive response to alleviate proteomic instability**
197 We next asked why cells attenuate protein translation in response to HSF1 deficiency. While
198 HSF1 maintains protein quality through HSPs, mTORC1 regulates protein quantity by
199 controlling translation. Because it is beneficial to lower protein quantity when protein quality is
200 compromised, we reasoned that this regulation represents a cellular adaptive response to the
201 imbalance between protein quantity and quality induced by HSF1 deficiency.
202
203 Proteomic imbalance disrupts proteome homeostasis and promotes proteomic instability, which
204 may ultimately trigger amyloidogenesis. To induce proteomic imbalance, we first stimulated
205 protein translation in MPNST cells by inhibiting JNK. As expected, treatment with JNK-IN-8
206 effectively reduced phosphorylation of c-JUN, a canonical JNK substrate,[34] in MPNST cells

207 (Figure 4A). Consistent with enhanced protein translation, JNK-IN-8 further activated mTORC1
208 signaling in these cells (Figures 4A and S4A). In contrast, only minimal effects were observed in
209 HSCs (Figure 4B), in line with their low basal JNK activity, as evidenced by unchanged c-JUN
210 phosphorylation. Intriguingly, the heightened protein translation following JNK inhibition was
211 accompanied by elevated amyloid accumulation in MPNST cells (Figures 4C and S4B), whereas
212 no significant changes were observed in HSCs (Figure 4D).
213
214 To directly assess the role of protein translation in amyloidogenesis, we inhibited translation
215 using two pharmacological agents with distinct mechanisms of action: 4EGI-1, which disrupts
216 eIF4E–eIF4G interactions,[39] and LY2584702, an inhibitor of p70S6K.[40] Both compounds
217 reduced basal amyloid levels in MPNST cells (Figures 4E,4F, and S4C), establishing a causal
218 link between protein translation and amyloidogenesis. Furthermore, translation inhibition
219 abrogated the induction of amyloids by JNK-IN-8 in MPNST cells (Figures 4G, 4H, S4D, and
220 S4E), indicating that JNK suppresses amyloidogenesis by inhibiting translation. No significant
221 effects were observed in HSCs (Figures 4G and 4H).
222
223 Given this relationship, we reasoned that preventing translation attenuation would aggravate
224 proteomic imbalance and enhance cytotoxicity in malignant cells. Consistent with this notion,
225 JNK inhibition by JNK-IN-8 further elevated amyloid levels in *HSF1*-depleted MPNST cells,
226 accompanied by exacerbated apoptosis as evidenced by caspase 3 cleavage (Figures 4I, 4J, and
227 S4F).[41] Notably, CR treatment suppressed this apoptosis, as indicated by reduced PARP cleavage
228 (Figure S4G),[42] causally implicating amyloidogenesis in this cell death. In contrast, *HSF1*
229 depletion and JNK inhibition had minimal effects on non-transformed Schwann cells (Figures

230 4K and 4L), consistent with their balanced proteome and low propensity for amyloid formation.
231 Together, these findings demonstrate that proteomic imbalance in malignant cells drives
232 proteomic instability and amyloidogenesis, leading to cytotoxicity. In non-transformed cells,
233 balanced protein quantity and quality prevent such instability. Thus, attenuation of protein
234 translation represents an adaptive mechanism by which cancer cells mitigate proteotoxic stress
235 and survive proteomic imbalance (Figure 4M).
236
237 **mTORC1 stimulation aggravates proteomic imbalance and cytotoxicity induced by HSF1**
238 **inhibition**
239 Because JNK regulates multiple targets beyond mTORC1, we sought to stimulate mTORC1 and
240 protein translation specifically. To this end, we genetically inhibited the tumor suppressor
241 Tuberous Sclerosis Complex subunit 2 (*TSC2*), a key negative regulator of mTORC1,[43] in
242 MPNST cells. As expected, *TSC2* knockdown in MPNST cells increased phosphorylation of
243 both p70S6K and 4EBP1, indicative of mTORC1 activation, which was accompanied by
244 elevated amyloid levels (Figures S5A-S5F). Like genetic *HSF1* depletion, pharmacological
245 inhibition of HSF1 with DTHIB— a small-molecule inhibitor that binds the HSF1 DNA-binding
246 domain to block transcription[44] —elevated global protein polyubiquitination and amyloids in
247 MPNST cells (Figures 5A, 5B, and S5G), indicating proteomic instability. Notably, HSF1
248 inhibition induced considerably greater amyloid accumulation in *TSC2*-deficient cells than in
249 control cells (Figure 5B), suggesting that elevated protein translation exacerbates proteotoxic
250 stress. *TSC2*-deficient cells also exhibited heightened JNK activation and mTORC1 inhibition
251 following DTHIB treatment, reflecting an amplified cellular response to severe proteotoxic
252 stress. Correspondingly, whereas control MPNST cells showed only modest cytotoxicity upon

253 HSF1 inhibition, measured by plasma membrane permeabilization, *TSC2*-deficient cells were
254 markedly more sensitive (Figures 5C, 5D, and S5H-S5K). Importantly, either inhibition of
255 protein translation or blockade of amyloid formation with CR largely rescued this cytotoxicity
256 (Figures 5C and 5D), causally implicating proteomic instability and amyloidogenesis in this cell
257 death. In support of a role for HSF1 in enabling *TSC2* deficiency, in tumors harboring *TSC2*
258 deletion higher *HSF1* gene expression correlates with poorer patient survival (Figure S5L).
259
260 To exclude potential mTORC1-independent effects of *TSC2* deficiency, we stimulated mTORC1
261 using NV-5138, a leucine analog currently in clinical trials as an antidepressant.[45,46]Amino acids,
262 particularly leucine, are potent activators of mTORC1.[47] Of note, although NV-5138 activates
263 mTORC1, it cannot be incorporated into protein synthesis.[45,46] To maximize mTORC1 activation
264 *ex vivo*, cells were cultured in leucine-free medium. Similar to *TSC2* knockdown, NV-5138
265 stimulated mTORC1 and elevated amyloid levels in MPNST cells (Figures S5M and 5E).
266 However, it elicited pronounced cytotoxicity only when combined with HSF1 inhibition, which
267 was largely rescued by CR treatment (Figure 5F). In contrast, combined NV-5138 and DTHIB
268 treatment had minimal effects on non-transformed Schwann cells (Figure 5G), consistent with
269 their reduced responsiveness to mTORC1 stimulation (Figures S5N). We next reasoned that by
270 directly contributing to protein quantity, L-leucine might impact the cancer proteome more
271 profoundly. In both S462 and 90-8TL cells, L-leucine synergized with DTHIB to induce severe
272 cytotoxicity (Figures 5H and S5O), whereas no cytotoxicity was induced in HSCs (Figure 5I).
273
274 To further corroborate the HSF1-dependent effects of DTHIB, we tested an independent small-
275 molecule inhibitor, KRIBB11[48], which binds the HSF1 transactivation domain to block the

276 recruitment of pTEFb. KRIBB11, consistent with DTHIB, synergized with L-leucine to promote
277 amyloid formation and trigger severe cytotoxicity in MPNST cells; importantly, CR treatment
278 both diminished amyloid levels and blocked cell death (Figures 5J and 5K). Finally, genetic
279 depletion of *HSF1* using shRNAs similarly synergized with L-leucine stimulation to provoke
280 prominent cytotoxicity (Figure 5L), providing orthogonal validation.
281
282 Collectively, these findings demonstrate that mTORC1 stimulation synergizes with HSF1
283 inhibition to drive severe cytotoxicity in cancer cells. This effect is mediated, at least in part, by
284 unconstrained proteomic imbalance and amyloidogenesis.
285
286 **Unconstrained proteomic imbalance incites pronounced cell death**
287 HSF1 inhibition alone induced both apoptotic and non-apoptotic death in MPNST cells, as
288 indicated by the presence or absence of caspase 3 cleavage. Intriguingly, concurrent mTORC1
289 stimulation shifted cell death predominantly toward a non-apoptotic mode, characterized by
290 plasma membrane permeabilization without caspase 3 cleavage (Figures 6A and 6B).
291
292 Multiple forms of non-apoptotic cell death, including pyroptosis, necroptosis, ferroptosis, and
293 autophagic cell death, can lead to loss of membrane integrity. To define the mechanism, we first
294 tested the role of caspases. Corroborating a caspase-independent mechanism, the pan-caspase
295 inhibitor Q-VD-OPh failed to prevent membrane permeabilization in *TSC2*-deficient MPNST
296 cells treated with the HSF1 inhibitor DTHIB (Figures 6A and 6B).[49] In contrast, Q-VD-OPh
297 effectively blocked apoptosis in control MPNST cells (Figures 6A and S6A), confirming its
298 activity. Because Q-VD-OPh also inhibits caspase 1 and no caspase 1 cleavage was detected

299 (Figure S6B),[50] a key mediator of pyroptosis,[51] these results argue against pyroptotic cell death.
300 Similarly, HSF1 inhibition did not induce necroptosis in *TSC2*-deficient MPNST cells, as
301 indicated by the absence of MLKL Ser358 phosphorylation (Figure S6B), a hallmark of
302 necroptotic execution.[52] Congruently, the necroptosis inhibitor necrostatin-1 had no effects on
303 membrane permeabilization (Figures 6C and S6C).[52]
304
305 Intriguingly, HSF1 inhibition in *TSC2*-deficient MPNST cells decreased glutathione peroxidase
306 4 (GPX4) but increased transferrin receptor 1 (TFR1), accompanied by markedly elevated lipid
307 peroxidation (Figures 6D and S6D), features typically associated with ferroptosis.[53,54] However,
308 the ferroptosis inhibitor liproxstatin-1,[53,54] while effectively reversing TFR1 elevation induced by
309 the ferroptosis inducer erastin, failed to suppress either TFR1 upregulation or membrane
310 permeabilization triggered by DTHIB (Figures 6C, 6D, and S6C). These results are not due to
311 ineffective inhibition, as both necrostatin-1 and liproxstatin-1 robustly blocked necroptosis and
312 ferroptosis, respectively, in control HT-29 cells (Figure S6E). HSF1 inhibition also elicited
313 autophagy, as evidenced by diminished p62/SQSTM1 and increased LC3B-II levels (Figure
314 6E).[55] To assess whether autophagy contributes to cell death, we blocked autophagy using the
315 class III PI3K inhibitor wortmannin.[56] Wortmannin effectively blocked autophagic flux, as
316 shown by reversal of rapamycin-induced changes in p62/SQSTM1 and LC3B-II (Figure 6E),
317 confirming successful inhibition of autophagy. Nevertheless, it failed to prevent membrane
318 permeabilization in *TSC2*-deficient cells treated with HSF1 inhibitors (Figures 6F and S6F).
319 These findings indicate that ferroptosis- and autophagy-associated changes occur downstream of
320 severe proteotoxic stress and are not the primary causes of cell death. Instead, our data support a
321 model in which unrestrained proteomic instability and consequent amyloidogenesis trigger a

322 unique form of cell death that is independent of apoptosis, autophagy, and canonical
323 programmed necrosis pathways (Figure 6G). We term this process proteomic catastrophe-
324 induced death (PCID). While its precise molecular execution remains to be fully defined, PCID
325 represents a mechanistically distinct vulnerability arising from the collapse of proteome
326 homeostasis in cancer cells.
327
328 **Unconstrained proteomic imbalance suppresses *in vivo* tumor growth**
329 Due to the limited *in vivo* bioavailability of DTHIB in our mouse models, we employed
330 KRIBB11 for *in vivo* studies. In agreement with our *ex vivo* findings, combined L-leucine
331 supplementation and KRIBB11 administration significantly suppressed the growth of
332 xenografted human S462 MPNST tumors in immunocompromised mice (Figure 7A). Despite
333 this overall reduction in tumor burden, 2 out of 8 tumors did not respond to the combination
334 treatment (Figure S7A), resulting in notable variations and a right-skewed distribution. Notably,
335 KRIBB11 alone only marginally affected tumor growth; conversely, in the presence of leucine it
336 markedly slowed tumor exponential growth rates and delayed tumor volume doubling time
337 (Figures S7B). This combination treatment also trended toward improved survival (Figure S7C).
338
339 To evaluate the broader applicability of this therapeutic strategy, we established a syngeneic
340 mouse melanoma model using B16-F10 cells in C57BL/6J mice. Similar to the MPNST model,
341 combined KRIBB11 and L-leucine supplementation significantly impeded tumor growth in this
342 aggressive model (Figures 7B and S7D). As expected, L-leucine activated mTORC1 signaling,
343 as indicated by increased S6RP phosphorylation (Figure 7C). Successful inhibition of HSF1 by
344 KRIBB11 was confirmed by the reduced transcription of *Hspa1a/Hsp72* and *Hspb1/Hsp25*

345 within the tumors (Figure 7D). Significantly, the combination treatment markedly induced
346 amyloid accumulation within tumors (Figure 7E). In stark contrast, no amyloids were induced in
347 normal tissues, including the brain and spleen (Figures 7F and 7G). Moreover, these treatments
348 did not cause significant loss of body weight (Figure S7E). In aggregate, these *in vivo* findings
349 from two distinct mouse models demonstrate that enforced proteomic imbalance—achieved
350 through combined HSF1 inhibition and mTORC1 stimulation—induces proteomic catastrophe
351 that suppresses tumor growth while sparing normal tissues (Figure 7H).
352
353
354
355
356
357
358
359
360
361
362
363
364
365
366
367

368 **DISCUSSIONS**

369 Genomic instability is widely recognized as a fundamental driver of oncogenesis. In contrast, the
370 role of proteomic instability in cancer remains obscure.

371

372 **Proteomic instability is tumor suppressive yet inevitable**

373 Proteomic instability does occur in cancer, as evidenced by elevated protein polyubiquitination,
374 aggregation, and even amyloidogenesis. Multiple factors contribute to this instability, including
375 protein oxidation by reactive oxygen species, mutation-induced protein misfolding, and
376 increased protein dosage resulting from aneuploidy.[1,3] Our recent findings further identify
377 uncontrolled protein translation as a key contributor to amyloidogenesis. This is not entirely
378 surprising, as it is estimated that up to 30% of newly synthesized polypeptides are misfolded and
379 targeted for proteasomal degradation.[57] Aberrant protein synthesis is therefore likely to increase
380 the burden of misfolded proteins, promoting protein aggregation and amyloid formation—
381 particularly in cancer cells, which harobor numerous mutations affecting protein folding.
382 Heightened protein translation, paradoxically, is also essential for malignant growth, rendering
383 proteomic instability and amyloidogenesis an unavoidable consequence of oncogenesis.

384

385 At the cellular level, amyloids are toxic to both neurons and cancer cells. At the organismal
386 level, while amyloidogenesis contributes to neurodegeneration, it appears to exert tumor-
387 suppressive effects. Mechanistically, our findings demonstrate that soluble AOs can directly
388 target HSP60, a key guardian of the mitochondrial proteome. It is likely that additional targets
389 and mechanisms contribute to amyloid toxicity in cancer. Moreover, the composition of cancer-
390 associated amyloids remains largely undefined. Beyond well-characterized species such as

391 Alzheimer's disease-associated Aβ, identifying the proteins that form amyloids in cancer will be
392 critical for understanding their functional roles and therapeutic potential.
393
394 **HSF1 contains proteomic instability to enable malignancy**
395 The diverse pro-oncogenic functions of HSF1 have been attributed to a wide array of
396 mechanisms; nonetheless, a unifying principle has remained elusive.
397
398 As an inherent consequence of malignant transformation, proteomic instability must be
399 restrained to avert tumor suppression and sustain cancer cell fitness. Now, our findings identify
400 containment of proteomic instability—particularly amyloidogenesis—as a central, unifying pro-
401 oncogenic function of HSF1. Notably, HSF1 does not eliminate amyloid formation but instead
402 limits its extent and toxicity. This is consistent with the fact that uncontrolled protein translation,
403 a hallmark of cancer, continuously drives amyloidogenesis. Consequently, cancer cells become
404 dependent on HSF1 to buffer this intrinsic proteotoxic burden, providing a mechanistic basis for
405 "HSF1 addiction".
406
407 Mechanistically, HSF1 contains amyloidogenesis through both indirect and direct means.
408 Indirectly, HSF1 induces HSPs to ensures proper protein folding and maintain proteome
409 integrity, thereby limiting the generation of misfolded proteins and amyloids. This is supported
410 by the observation that HSF1 inhibition leads to increased protein ubiquitination, aggregation,
411 and amyloid accumulation. Directly, HSF1 neutralizes soluble AOs once they form. With HSF1
412 inhibition, AOs are free to target HSP60, compromising the mitochondrial proteome and
413 triggering cytoxicity. Thus, in cancer cells HSF1 inhibition not only increases the burden of

414 amyloids but, critically, exposes their intrinsic toxicity. Together, these findings establish that
415 HSF1 enables malignancy by buffering proteomic instability, positioning it as a central safeguard
416 against proteotoxic collapse in cancer cells.
417
418 **mTORC1 signaling becomes tumor suppressive in the absence of HSF1**
419 Given the fundamental dependency of malignant growth on protein translation, mTORC1
420 signaling is frequently hyperactivated in human cancers and is traditionally viewed as
421 oncogenic.[58,59] However, our findings reveal a striking context-dependent shift: in the absence of
422 HSF1, mTORC1 signaling becomes tumor suppressive. This functional reversal arises from a
423 profound imbalance between protein quantity and quality. Without HSF1 to maintain proteome
424 integrity, continued mTORC1-driven protein synthesis exacerbates proteomic instability, leading
425 to enhanced amyloidogenesis and cytotoxicity. The observation that cytotoxicity is alleviated by
426 either translation inhibitors or blockade of amyloid formation with CR strongly supports this
427 model.
428
429 Conceptually, HSF1 enables the oncogenic potential of mTORC1 signaling by buffering the
430 proteotoxic stress associated with elevated protein synthesis. In its absence, mTORC1-driven
431 translation becomes detrimental, converting a canonical growth-promoting pathway into a tumor-
432 suppressive force. These findings further establish HSF1 as a critical oncogenic enabler that
433 permits cancer cells to tolerate the proteomic burden of malignant growth.
434
435 **Inducing proteomic catastrophe represents a next-generation therapeutic paradigm**

436 Conventional chemo- and radiotherapies primarily target the cancer genome by inducing DNA
437 damage. An emerging paradigm in oncology is to instead target the cancer proteome. To date,
438 most efforts have focused on inhibiting individual HSP families, such as HSP70 and HSP90.[60,61]
439 However, this strategy faces intrinsic limitations: cells harbor both constitutive HSPs, which
440 maintain essential basal proteostasis, and inducible HSPs, which provide additional chaperoning
441 capacity that is dispensable for basal proteostasis but required under stress. The structural and
442 functional similarity between these HSPs complicates selective targeting, and redundancy across
443 multiple HSP families further limits the efficacy of targeting any single chaperone system.
444
445 Our findings, together with prior studies, suggest that malignant cells operate under chronic
446 proteotoxic stress, resulting in constitutive HSF1 activation. Consequently, cancer cells become
447 reliant on the inducible chaperoning capacity governed by HSF1 for growth and survival.
448 Targeting HSF1 therefore represents a strategy to selectively disable this stress-adaptive reserve
449 while preserving basal proteostasis in normal cells. These insights provide a strong rationale for
450 therapeutic targeting of HSF1, an approach that is now beginning to enter clinical investigation.[62]
451
452 In response to HSF1 inhibition, cancer cells attenuate protein synthesis as an adaptive
453 mechanism, highlighting the importance of maintaining a balance between protein quantity and
454 quality. This observation led us to explore whether deliberately driving proteomic imbalance
455 could be therapeutically exploited.
456
457 Although mTORC1 hyperactivation is widespread in human cancers and has long been targeted
458 with inhibitors,[59, 63] these agents have largely produced cytostatic effects and limited clinical

benefit.[63,64] Moreover, because protein synthesis is essential for normal cellular function, systemic mTORC1 inhibition carries significant toxicity, including immunosuppression.[63,65]

In contrast to conventional approaches, we pursued a counterintuitive strategy: stimulating mTORC1 to drive proteomic imbalance. When combined with HSF1 inhibition, mTORC1 stimulation engenders catastrophic proteomic instability in cancer, culminating in cell death and tumor suppression (Figure 7G). This PCID offers a wider therapeutic window, as normal cells, with intact proteostasis and low proteotoxic stress, are largely spared. Mechanistically, mTORC1 activation increases protein synthesis, which can be accommodated in normal cells but overwhelms the already stressed proteome of cancer cells, particularly given their burden of mutant and misfolded proteins. Although cancer cells attempt to adapt via JNK-mediated suppression of mTORC1, further specific blockade of this adaptive response is expected to amplify proteomic imbalance and enhance therapeutic efficacy.

Transcription factors, traditionally, have been considered “undruggable” targets for small molecules. While prototype direct HSF1 inhibitors such as DTHIB and KRIBB11 provide important proof-of-concept, their limited *in vivo* potency underscores the need for more clinically viable compounds. Nonetheless, our study establishes a new therapeutic paradigm: the deliberate induction of proteomic catastrophe in cancer cells. We demonstrate a feasible strategy to achieve this by simultaneously disrupting proteome quality control and enhancing protein synthesis, thereby overwhelming the proteostatic capacity of malignant cells. This approach may be broadly applicable across tumor types and represents a promising next-generation strategy for cancer therapy.

ACKNOWLEDGMENTS

We would like to thank the Optical Microscopy and Image Analysis lab (OMAL) for their assistance with the confocal microscopy studies and Holly Morris for her assistance in animal studies. Schematic illustrations are created with BioRender.com. This work was supported by the grant from Department of Defense Congressionally Directed Medical Research Programs to C.D. (NF150028) and by the Intramural Research Program of the NIH, National Cancer Institute, Center for Cancer Research (1ZIABC011767). The content of this publication does not necessarily reflect the views or policies of the Department of Health and Human Services, nor does mention of trade names, commercial products, or organizations imply endorsement by the U.S. government.

AUTHOR CONTRIBUTIONS: B.M.R., O. S., and K-H.C. designed and conducted the experiments. C.D. conceptualized and supervised this study and analyzed the results. B.M.R. and C.D. wrote the manuscript.

DECLARATION OF INTERESTS: The authors declare no competing interests.

505 **EXPERIMENTAL MATERIALS AND METHODS**

506 **Cells, Chemicals, and reagents**

507 S462 (female) and 90-8TL (female) cells were kindly provided by Dr. Karen Cichowski.
508 sNF96.2 cells (male) and immortalized human Schwann cells (hTERT ipn02.3 2λ, female) were
509 purchased from ATCC. Primary human Schwann cells (Cat#1700, ScienCell Research
510 Laboratories) were grown on poly-L-lysine coated T-75 flasks and maintained in complete
511 Schwann Cell Medium (Cat#1701, ScienCell Research Laboratories). B16-F10-luc2 (male)
512 cells were purchased from ATCC (cat#CRL-6475-LUC2). All cell lines, except 90-8TL and
513 HSCs (no known STR profiles available), were authenticated by ATCC. All cell lines, except
514 primary human Schwann cells, were maintained in DMEM supplemented with 10% HyClone
515 bovine growth serum and 1% penicillin–streptomycin. Cells were maintained in an incubator
516 with 5% CO2 at 37 °C.

517

518 The following chemicals were purchased from commercial sources: JNK-IN-8 (Cat#S4901,
519 Selleckchem), 6-FAM-dC-puromycin (cat#NU-925-6FM, Jena Bioscience), Congo red
520 (cat#B2431014, Thermo Scientific Chemicals), Thioflavin T (cat#211760050, Thermo Scientific
521 Chemicals), LY2584702 (cat#S7698, Selleckchem), 4EGI-1 (cat#S7369, Selleckchem), and
522 DTHIB (cat# HY-138280, MedChemExpress), KRIBB11 (cat#HY-100872, MedChemExpress),
523 KRIBB11 (cat#T3652, TargetMol Chemicals), Q-VD-OPh (cat#HY-12305, MedChemExpress),
524 necrostatin-1 (cat#HY-15760, MedChemExpress), Liproxstatin-1 (cat#HY-12726,
525 MedChemExpress), wortmannin (cat#HY-10197, MedChemExpress), rapamycin (cat#HY-
526 10219, MedChemExpress), erastin (cat#HY-15763, MedChemExpress), MHY1485 (cat#HY-
527 B0795, MedChemExpress), NV-5138 HCl (cat#HY-114384B, MedChemExpress), and Liperfluo

528 (cat#L248, Dojindo Laboratories), dimethylacetamide (cat#T19439, TargetMol Chemicals
529 Inc.), PEG300 (cat#T7022, TargetMol Chemicals Inc.), and Captisol (cat#RC-0C7-100, CyDex
530 Pharmaceuticals).
531
532 Rabbit phospho-4EBP1 S65/T70 antibody (cat#sc-12884-R), mouse monoclonal HSF1 (E-4,
533 cat#sc-17757) antibody, rabbit HSF1 antibody (H-311, cat#sc-9144), mouse monoclonal JNK
534 (D-2, cat#sc-7345), rabbit JNK1/3 (C-17, cat#sc-474) antibody were purchased from Santa
535 Cruz Biotechnology; antibodies for phosphor-4EBP1 Thr70 (cat#9455), phospho-4EBP1
536 Thr37/46 (236B4, cat#2855), phospho-p70S6K T389 (108D2, cat# 9234), phosphor-S6RP
537 Ser235/236 (D57.2.2E, cat#4858), p70 S6K (49D7, cat#2708), 4EBP1 (53H11, cat#9644),
538 S6RP (5G10, cat#2217), mTOR (7C10, cat#2983), phospho-JNK1/2 T183/Y185 (81E11,
539 cat#4668), JNK2 (56G8, cat#9258), c-Jun (60A8, cat#9165), phospho-c-Jun Ser63 II
540 (cat#9261), PARP (cat#9542), Tuberin/TSC2 (D93F12, cat#4308), SQSTM1/p62 (D1Q5S,
541 cat#39749), cleaved caspase 3 (Asp175) (5A1E, cat#9664), caspase 1(D7F10, cat#3866),
542 gasdermin D (E9S1X, cat#39754), phosphor-MLKL Ser358 (D6H3V, cat#91689), GPX4
543 (E5Y8K, cat#59735), and transferrin receptor/CD71 (H68.4, cat#46222) antibody were
544 purchased from Cell Signaling Technologies; mouse β-actin antibody-HRP (Cat#A00730)
545 conjugates were from GenScript. Anti-K48-specific ubiquitin antibody (Apu2, cat#05-1307)
546 and mouse monoclonal anti-RAPTOR antibody (1H6.2, cat#05-1470) were purchased from
547 EMD Millipore. Mouse monoclonal anti-JNK1 (C-terminal region) antibody (cat#JM2671)
548 was purchased from ECM Biosciences. Anti-amyloid oligomers (A11, cat#SPC-506D) and
549 anti-amyloid fibrils (OC, cat#SPC-507D) antibodies were purchased from StressMarq
550 Biosciences Inc. Mouse monoclonal anti-HSP60 antibody (LK-1, cat#ADI-SPA-806) was

551 purchased from Enzo Life Sciences Inc. β-Actin (cat#GTX629630), GAPDH
552 (cat#GTX627408), α-tubulin (GT114, cat#GTX628802), and LC3B antibody
553 (cat#GTX127375) was purchased from GeneTex Inc.
554

555 **METHOD DETAILS**

556 **Lentiviral Particle Production and Transduction of lentiviral shRNAs**

557 Lentiviral pLKO.1 shRNA plasmids targeting human *HSF1* were described previously[10]:
558 TRCN0000007480 (hA6) and TRCN0000007483 (hA9). The sequence of control hairpins
559 targeting a scrambled sequence with no known homology to any human genes is 5′-
560 CCTAAGGTTAAGTCGCCCTCG-3′. The pLKO.1 shRNA plasmid targeting human *TSC2* was
561 a gift from Do-Hyung Kim (Cat#15478, Addgene). Lentiviral pLKO shRNA plasmids were
562 transiently co-transfected individually along with plasmids encoding ΔVPR and VSV-G into
563 HEK293T cells using TurboFect™ (Cat#R0531, Thermo Scientific). Viral supernatants were
564 collected after centrifugation at 1,000 rpm for 15 min. Viral transduction was achieved by
565 incubating target cells with viral supernatants containing 10μg/ml polybrene (Cat#TR-1003-G,
566 Millipore-Sigma) for 24h. For stable knockdown of *TSC2,* lentivirus particles were prepared using
567 pLKO shRNA plasmids targeting human *TSC2*. Scrambled shRNA was used for stable control
568 cells. After 4 days of transduction, cells were gradually selected using 1-4 μg/ml puromycin for 2
569 weeks.

570 **Soluble and Insoluble Protein Fractionation**

571 Equal numbers of cells were incubated with cold cell-lysis buffer (100 mM NaCl, 30 mM Tris-
572 HCl pH 7.6, 1% Triton X-100, 20 mM sodium fluoride, 1mM EDTA, 1mM sodium
573 orthovanadate, and 1x Halt™ protease inhibitor cocktail) on ice for 20 min. The crude lysates
574 were first centrifuged at 500xg for 5 min at 4°C. The supernatants from low-speed (500xg)
575 centrifugation were transferred to a new Eppendorf tube. The first pellets were resuspended in
576 DNA digestion solution (2 units DNase I, 1% Triton X-100, 10 mM Tris-HCl, 2.5 mM
577 MgCl2, 0.5 mM CaCl2, pH 7.6) for 30 min at RT. An equal volume of 1xPBS with 2% SDS
578 was then added to resuspend the first pellets for additional 30 min at RT. Following the
579 centrifugation at 17,000xg for 10 min at RT, the supernatants were removed. The supernatants
580 from low-speed centrifuge were added back to the second pellets, followed by centrifugation
581 at 17,000xg for 15 min at 4°C. The final supernatants and pellets from high-speed (17,000xg)
582 centrifugation were collected as detergent-soluble and -insoluble fractions, respectively.
583 Insoluble fractions were further sonicated in 1xPBS with 2% SDS at high intensity using a
584 Bioruptor® Sonication Device (Diagenode) for SDS-PAGE.

585 **ThT and CR Staining for Flow Cytometry**

586 After washing with 1xPBS, cells were fixed with 4% formaldehyde at RT for 10 min.
587 Following fixation and 1xPBS washing, cells were resuspended in 1 ml permeabilization
588 buffer (1xPBS with 0.5% Triton X-100 and 3 mM EDTA) and incubated on ice for 30 min.
589 Following washing with 1xPBS, Cells were stained with 10 μM ThT or CR dissolved in
590 1xPBS for 5 min. Cells were washed and resuspended in PBS and fluorescence signals were
591 measured by a FACSCalibur, LSRFortessa X-20 or LSR II flow cytometer (BD Biosciences).

592 **Amyloid Oligomer and Fibril Quantitation by Direct ELISA and Flow Cytometry**

593 To quantitate soluble amyloid prefibrillar oligomers, soluble cell lysates diluted in 1xPBS
594 from equal numbers of cells were coated on each well in a 96-well ELISA plate at 4°C
595 overnight followed by blocking (5% non-fat milk in TBS-0.05% Tween® 20) at RT for 1 hr.
596 Each well was incubated with 100 µl amyloid oligomer antibodies (A11, 1:1,000 diluted in
597 the blocking buffer) at RT for 2 hr. After washing with TBS-T, goat anti-rabbit secondary Ab
598 HRP conjugates (1:1,000 diluted in blocking buffer) were added to each well and incubated at
599 RT for 1 hr. Following washing, 100 µl 1-Step Ultra TMB-ELISA substrates (Cat#34029,
600 Thermo Scientific) were added to each well. After adding 100µl Stop solution, absorbance was
601 measured at 450 nm using a SpectraMax iD5 microplate reader (Molecular Devices).

602 To quantitate amyloid fibrils, detergent-insoluble fractions from equal numbers of cells were
603 extracted as described in Soluble and Insoluble Protein Fractionation. The final pellets were
604 collected as detergent-insoluble fractions and solubilized by sonication for 15 min in 1xPBS
605 with 2% SDS. Solubilized proteins diluted in 1xPBS were added to each well and incubated at
606 37°C without cover overnight to air dry the wells. The following steps were identical to the
607 oligomer detection except for the use of amyloid fibril antibodies (OC) as the primary Ab.

608 For amyloid oligomer and fibril quantification by flow cytometry, cells were collected by
609 trypsinization and fixed in 4% Formaldehyde at RT for 10 min. Following permeabilization using
610 0.3% Triton-X-100, samples were incubated with primary antibodies A11-FITC (1:100 in 5%
611 BSA, StressMarq Biosciences, cat# SPC-506D-FITC) or OC-PerCP (1:100 in 5% BSA,
612 StressMarq Biosciences, cat# SPC-507D-PCP) at RT for 3 hrs. The cells were washed with PBS
613 and analyzed using flow cytometry.

614
615

616 **Measurement of Cell Viability**

617 Cell viability was determined using the CellTiter-Blue® Cell Viability Assay (cat#G8080,
618 Promega). Cells were grown in 96 well plates (1×10^4 per well) for 24h. A 20µl CellTiter-Blue®
619 reagent was added to 100µl of media in each well. The plates were incubated for 2h at 37°C and
620 the fluorescence was recorded at 560/590 nm. The reagents were discarded, and the wells were
621 washed with PBS before adding fresh media. Similarly, subsequent readings were recorded at
622 24h intervals till 96h time point.

623

624 **Proximity Ligation Assay**

625 Cells were fixed with 4% formaldehyde in PBS for 15 min at RT. After blocking with 5% normal
626 goat serum in PBS with 0.3% Triton X-100, primary antibodies 1:100 diluted in blocking buffer
627 were incubated with fixed cells overnight at 4°C. Following washing with PLA wash Buffer A,
628 samples were incubated with 1:5 diluted Duolink® in Situ PLA Probe anti-rabbit Plus
629 (cat#DUO92002, Sigma-Aldrich) and anti-mouse Minus (cat#DUO92004, Sigma-Aldrich) at
630 37°C for 1 hr. Subsequently, ligation (30 minutes, 37°C), rolling circle amplification, and detection
631 (120 minutes, 37°C) were performed using the Duolink® In Situ Detection Reagents Red
632 (cat#DUO92008, Sigma-Aldrich). Nuclei were counterstained with Hoechst 33342. PLA
633 signals were documented by a Zeiss LSM780 confocal microscope (Carl Zeiss). For PLA flow
634 cytometry, an equal number of cells were collected in microcentrifuge tubes by trypsinization and
635 fixed with 4% formaldehyde in PBS for 10 min at RT. Subsequent PLA steps were followed as
636 described earlier. The PLA signals were quantified by a FACSCalibur flow cytometer (BD
637 Biosciences).

638

639 Mouse anti-JNK1 (JM2671) and rabbit anti-HSF1 (H-311) antibodies were used for JNK-HSF1
640 PLA. Rabbit anti-JNK1/3 (C-17) and mouse anti-RAPTOR (1H6.2) antibodies were used for
641 JNK-RAPTOR PLA. Rabbit anti-mTOR (7C10) and mouse anti-RAPTOR (1H6.2) antibodies
642 were used for mTOR-RAPTOR PLA. Mouse anti-HSF1 (E-4) and rabbit anti-AO (A11)
643 antibodies were used for HSF1-AO PLA. Rabbit anti-AO (A11) and mouse anti-HSP60 (LK1)
644 antibodies were used for AO-HSP60 PLA.

645 **Measurement of global protein translation**

646 Live cells were incubated with 100 nM 6-FAM-dC-puromycin in complete culture medium
647 for 30 min and analyzed by a FACSCalibur flow cytometer (BD Biosciences).

648

649 **Immunoblotting and Immunoprecipitation**

650 Whole-cell protein extracts were prepared in cold cell-lysis buffer (100 mM NaCl, 30 mM Tris-
651 HCl pH 7.6, 1% Triton X-100, 20 mM sodium fluoride, 1mM EDTA, 1mM sodium
652 orthovanadate, and 1x Halt™ protease inhibitor cocktail). Proteins were transferred to
653 nitrocellulose membranes. Following incubation with the blocking buffer (5% non-fat milk in 1x
654 TBS-T) for 1 hour at RT, membranes were incubated with primary antibodies (1:1,000 dilution in
655 the blocking buffer) overnight at 4 °C. After washing with 1xTBS-T for 3 times, membranes
656 were incubated with peroxidase-conjugated secondary antibodies (1: 3,000 diluted in the
657 blocking buffer) at RT for 1 hr. Signals were detected using SuperSignal™ West
658 chemiluminescent substrates. For normal Co-IP, proteins were extracted using a QSonica Q125
659 sonicator (total process time: 15S, pulse-on time: 5S, pulse-off time: 10S, output intensity: 30%)
660 in 1x sonication buffer (20 mM Tris, 20 mM NaCl, 1 mM EDTA, 20 mM β-glycerol-phosphate,

661 20 mM sodium fluoride, 4 mM sodium orthovanadate, and 1 mM DTT pH7.4, supplemented
662 with Halt protease inhibitor cocktail). Total 1 mg whole cell lysates were incubated with A11
663 antibodies at 4 °C overnight. Normal rabbit IgG were used as the negative controls. The primary
664 antibody was precipitated using Protein G magnetic beads. After washing with the lysis buffer
665 for 3 times, beads were boiled in 1x loading buffer for 5 min before loading on SDS-PAGE.
666 EasyBlocker (Cat#GTX425858, GeneTex) was used for blocking and anti-HSF1 (H-311)
667 primary antibody (cat#sc-9144, Santa Cruz Biotechnology) incubation (1:1,000, O/N at 4°C).
668 The blot was incubated with EasyBlot anti-Rabbit IgG HRP conjugated antibody
669 (cat#GTX221666-01, GeneTex) for 1 hour. Chemiluminescent signals were captured by an
670 iBright™ FL1000 imaging system (ThermoFisher Scientific).
671
672 **Live-Or-Dye™ Dead Cell Staining**
673 Cells were cultured in DMEM for 48 hours before being treated with inhibitors for the required
674 periods and collected by trypsinization. $1x10^6$ cells/ml cells were stained with Live-or-Dye™
675 fixable dead cell dyes (1:1,000 dilution, cat#32003, Biotium) at RT for 30 min, protected from
676 light. Stained cells were washed once with PBS and analyzed by flow cytometry. For co-staining
677 with cleaved caspase 3 antibody, stained cells were fixed with 4% formaldehyde (10 min, RT)
678 and permeabilized with 0.3% Triton-X-100 in PBS (10 min, RT). The cells were stained by
679 Cleaved Caspase 3 antibody (Asp175) (5A1E) (1:1,000, cat#9664, Cell Signaling Technology)
680 followed by goat anti-Rabbit IgG Alexa Fluor™ 488 conjugated (1:1,000, cat#A-11034,
681 ThermoFisher Scientific) secondary antibodies. The samples were analyzed by flow cytometry.

682 **Inhibitor treatments**

683 Treatments with DTHIB, Q-VD-OPh, Liproxstatin-1, Necrostatin-1, and Wortmannin were
684 done for 72 hours. For Congo Red and LY-2584702 treatments, cells were pretreated for 24h
685 followed by DTHIB for an additional 72h. For treatments with NV-5138, cells were pretreated
686 for 48 hours in a leucine-free DMEM (cat#226-024, Crystalgen) before adding DTHIB for an
687 additional 72 hours.

688

689 **Animal studies**

690 All animal experiments described here were approved by the institutional Animal Care and Use
691 Committee (ACUC) of the National Cancer Institute, Frederick. Experiments on all animals
692 were conducted following the recommendations of the Guide for the Care and Use of
693 Laboratory Animals (National Academies Press, 2011). Animals were housed and maintained
694 on a 12-hour light/12-hour dark cycle at temperatures between 20°C and 27°C and humidity
695 levels of 30% to 70%, with food and water *available ad libitum*.

696 To establish the MPNST xenograft model, $9x10^6$ S462 MPNST cells (female) suspended with 30
697 % Matrigel were subcutaneously implanted the right flanks of 8-week-old female NIH-III nude
698 mice (Charles River Laboratories). After 7 days, xenografted mice were assigned to 4 groups,
699 eight each group, by stratified randomization based on tumor sizes (between 72 and 199 mm^3).
700 Mice were treated with KRIBB11 (65mg/kg, i.p. injection daily, cat#HY-100872, Lot#317606,
701 Medchemexpress LLC) with and without 2% L-leucine dissolved in drinking water stored in
702 amber-colored bottles. KRIBB11 was freshly dissolved daily in the vehicle (final
703 concentration:10% dimethylacetamide, 50% PEG300, 20% Captisol, and 20% sterile saline).

704

705 To establish the syngeneic melanoma model, 2 × 10^6 B16-F10-luc2 cells (male) mixed with
706 Matrigel (1:1 ratio) in a 200μL volume were subcutaneously implanted into the right flanks of
707 8-week-old C57BL/6J male mice (The Jackson Laboratory). After 5 days, xenografted mice were
708 assigned to 4 groups, eight each group, by stratified randomization based on tumor sizes (between
709 75 and 284 mm^3). Mice were treated with KRIBB11 (65 mg/kg, i.p. injection daily, cat#T3652,
710 Lot#132988, TargetMol Chemicals Inc.) with and without 2% L-leucine dissolved in drinking
711 water stored in amber-colored bottles. KRIBB11 was freshly dissolved daily in the vehicle (final
712 concentration:10% dimethylacetamide, 50% PEG300, 16% Captisol, and 24% sterile saline).

713 To formulate the KRIBB11 solution, KRIBB11 was first dissolved in dimethylacetamide,
714 followed by addition of PEG300. Lastly, 40 or 50% Capitol dissolved in sterile saline was added.
715 Tumor sizes were measured using a caliper by an animal technician blind to the study. To
716 assess the compound's toxicity, the body weight of tumor-bearing animals was also recorded.
717 Tumor volumes were estimated using the formula [length (mm) × $width^2$ (mm^2)]/2.
718

719 **Quantification And Statistical Analysis**

720 Statistical analyses were performed using Prism GraphPad 10.0 (GraphPad Software). The
721 detailed statistical methods and sample sizes are provided in the figure legends. All results are
722 expressed as mean±SD, mean±SEM, or median and IQR. The statistical significance is defined
723 as: *$p<0.05$, **$p<0.01$; ***$p<0.001$; ****$p<0.0001$; n.s.: not significant. For *in vitro*
724 experiments, sample size required was not determined a priori. The experiments were not
725 randomized**.** For *in vivo* experiments, sample size required was determined by pilot experiments.
726

727 **REFERENCES**

728 1. Dai C, Dai S, Cao J. Proteotoxic stress of cancer: implication of the heat-shock response in
729 oncogenesis. J Cell Physiol. 2012;227(8):2982-7. doi: 10.1002/jcp.24017. PubMed PMID:
730 22105155; PMCID: PMC3431153.
731 2. Dai C. The heat-shock, or HSF1-mediated proteotoxic stress, response in cancer: from
732 proteomic stability to oncogenesis. Philos Trans R Soc Lond B Biol Sci. 2018;373(1738). doi:
733 10.1098/rstb.2016.0525. PubMed PMID: 29203710; PMCID: PMC5717525.
734 3. Guang MHZ, Kavanagh EL, Dunne LP, Dowling P, Zhang L, Lindsay S, Bazou D, Goh CY,
735 Hanley C, Bianchi G, Anderson KC, O'Gorman P, McCann A. Targeting Proteotoxic Stress in
736 Cancer: A Review of the Role that Protein Quality Control Pathways Play in Oncogenesis.
737 Cancers (Basel). 2019;11(1). Epub 20190109. doi: 10.3390/cancers11010066. PubMed
738 PMID: 30634515; PMCID: PMC6356294.
739 4. Wilson DM, 3rd, Cookson MR, Van Den Bosch L, Zetterberg H, Holtzman DM, Dewachter I.
740 Hallmarks of neurodegenerative diseases. Cell. 2023;186(4):693-714. doi:
741 10.1016/j.cell.2022.12.032. PubMed PMID: 36803602.
742 5. Tang Z, Dai S, He Y, Doty RA, Shultz LD, Sampson SB, Dai C. MEK guards proteome
743 stability and inhibits tumor-suppressive amyloidogenesis via HSF1. Cell. 2015;160(4):729-44.
744 doi: 10.1016/j.cell.2015.01.028. PubMed PMID: 25679764; PMCID: PMC4564124.
745 6. Li J, Labbadia J, Morimoto RI. Rethinking HSF1 in Stress, Development, and Organismal
746 Health. Trends Cell Biol. 2017;27(12):895-905. Epub 20170907. doi:
747 10.1016/j.tcb.2017.08.002. PubMed PMID: 28890254; PMCID: PMC5696061.
748 7. Anckar J, Sistonen L. Regulation of HSF1 function in the heat stress response: implications in
749 aging and disease. Annu Rev Biochem. 2011;80:1089-115. doi: 10.1146/annurev-biochem-

750 060809-095203. PubMed PMID: 21417720.

751 8. Gomez-Pastor R, Burchfiel ET, Thiele DJ. Regulation of heat shock transcription factors and
752 their roles in physiology and disease. Nat Rev Mol Cell Biol. 2018;19(1):4-19. Epub
753 20170830. doi: 10.1038/nrm.2017.73. PubMed PMID: 28852220; PMCID: PMC5794010.

754 9. Min JN, Huang L, Zimonjic DB, Moskophidis D, Mivechi NF. Selective suppression of
755 lymphomas by functional loss of Hsf1 in a p53-deficient mouse model for spontaneous
756 tumors. Oncogene. 2007;26(35):5086-97. Epub 20070219. doi: 10.1038/sj.onc.1210317.
757 PubMed PMID: 17310987.

758 10. Dai C, Whitesell L, Rogers AB, Lindquist S. Heat shock factor 1 is a powerful multifaceted
759 modifier of carcinogenesis. Cell. 2007;130(6):1005-18. doi: 10.1016/j.cell.2007.07.020.
760 PubMed PMID: 17889646; PMCID: PMC2586609.

761 11. Meng L, Gabai VL, Sherman MY. Heat-shock transcription factor HSF1 has a critical role in
762 human epidermal growth factor receptor-2-induced cellular transformation and
763 tumorigenesis. Oncogene. 2010;29(37):5204-13. Epub 20100712. doi:
764 10.1038/onc.2010.277. PubMed PMID: 20622894; PMCID: PMC2940982.

765 12. Jin X, Moskophidis D, Mivechi NF. Heat shock transcription factor 1 is a key determinant of
766 HCC development by regulating hepatic steatosis and metabolic syndrome. Cell Metab.
767 2011;14(1):91-103. doi: 10.1016/j.cmet.2011.03.025. PubMed PMID: 21723507; PMCID:
768 PMC3214631.

769 13. Dai C, Santagata S, Tang Z, Shi J, Cao J, Kwon H, Bronson RT, Whitesell L, Lindquist S.
770 Loss of tumor suppressor NF1 activates HSF1 to promote carcinogenesis. J Clin Invest.
771 2012;122(10):3742-54. Epub 20120904. doi: 10.1172/JCI62727. PubMed PMID: 22945628;
772 PMCID: PMC3461912.

773 14. Kourtis N, Lazaris C, Hockemeyer K, Balandran JC, Jimenez AR, Mullenders J, Gong Y,
774 Trimarchi T, Bhatt K, Hu H, Shrestha L, Ambesi-Impiombato A, Kelliher M, Paietta E,
775 Chiosis G, Guzman ML, Ferrando AA, Tsirigos A, Aifantis I. Oncogenic hijacking of the
776 stress response machinery in T cell acute lymphoblastic leukemia. Nat Med.
777 2018;24(8):1157-66. Epub 20180723. doi: 10.1038/s41591-018-0105-8. PubMed PMID:
778 30038221; PMCID: PMC6082694.
779 15. Fujimoto M, Takii R, Matsumoto M, Okada M, Nakayama KI, Nakato R, Fujiki K, Shirahige
780 K, Nakai A. HSF1 phosphorylation establishes an active chromatin state via the TRRAP-
781 TIP60 complex and promotes tumorigenesis. Nat Commun. 2022;13(1):4355. Epub
782 20220729. doi: 10.1038/s41467-022-32034-4. PubMed PMID: 35906200; PMCID:
783 PMC9338313.
784 16. Heimberger T, Andrulis M, Riedel S, Stuhmer T, Schraud H, Beilhack A, Bumm T, Bogen
785 B, Einsele H, Bargou RC, Chatterjee M. The heat shock transcription factor 1 as a potential
786 new therapeutic target in multiple myeloma. Br J Haematol. 2013;160(4):465-76. Epub
787 20121218. doi: 10.1111/bjh.12164. PubMed PMID: 23252346.
788 17. Chuma M, Sakamoto N, Nakai A, Hige S, Nakanishi M, Natsuizaka M, Suda G, Sho T,
789 Hatanaka K, Matsuno Y, Yokoo H, Kamiyama T, Taketomi A, Fujii G, Tashiro K, Hikiba Y,
790 Fujimoto M, Asaka M, Maeda S. Heat shock factor 1 accelerates hepatocellular carcinoma
791 development by activating nuclear factor-kappaB/mitogen-activated protein kinase.
792 Carcinogenesis. 2014;35(2):272-81. Epub 20131015. doi: 10.1093/carcin/bgt343. PubMed
793 PMID: 24130164.
794 18. Fujimoto M, Takaki E, Takii R, Tan K, Prakasam R, Hayashida N, Iemura S, Natsume T,
795 Nakai A. RPA assists HSF1 access to nucleosomal DNA by recruiting histone chaperone

796 FACT. Mol Cell. 2012;48(2):182-94. Epub 20120830. doi: 10.1016/j.molcel.2012.07.026.
797 PubMed PMID: 22940245.
798 19. Solimini NL, Luo J, Elledge SJ. Non-oncogene addiction and the stress phenotype of cancer
799 cells. Cell. 2007;130(6):986-8. doi: 10.1016/j.cell.2007.09.007. PubMed PMID: 17889643.
800 20. Gutmann DH, Ferner RE, Listernick RH, Korf BR, Wolters PL, Johnson KJ.
801 Neurofibromatosis type 1. Nat Rev Dis Primers. 2017;3:17004. Epub 20170223. doi:
802 10.1038/nrdp.2017.4. PubMed PMID: 28230061.
803 21. Hirbe AC, Gutmann DH. Neurofibromatosis type 1: a multidisciplinary approach to care.
804 Lancet Neurol. 2014;13(8):834-43. doi: 10.1016/S1474-4422(14)70063-8. PubMed PMID:
805 25030515.
806 22. Cichowski K, Jacks T. NF1 tumor suppressor gene function: narrowing the GAP. Cell.
807 2001;104(4):593-604. doi: 10.1016/s0092-8674(01)00245-8. PubMed PMID: 11239415.
808 23. Grice GL, Nathan JA. The recognition of ubiquitinated proteins by the proteasome. Cell Mol
809 Life Sci. 2016;73(18):3497-506. Epub 20160502. doi: 10.1007/s00018-016-2255-5. PubMed
810 PMID: 27137187; PMCID: PMC4980412.
811 24. Knowles TP, Vendruscolo M, Dobson CM. The amyloid state and its association with protein
812 misfolding diseases. Nat Rev Mol Cell Biol. 2014;15(6):384-96. doi: 10.1038/nrm3810.
813 PubMed PMID: 24854788.
814 25. Yakupova EI, Bobyleva LG, Vikhlyantsev IM, Bobylev AG. Congo Red and amyloids:
815 history and relationship. Biosci Rep. 2019;39(1). Epub 20190115. doi:
816 10.1042/BSR20181415. PubMed PMID: 30567726; PMCID: PMC6331669.
817 26. Kayed R, Head E, Thompson JL, McIntire TM, Milton SC, Cotman CW, Glabe CG.
818 Common structure of soluble amyloid oligomers implies common mechanism of

819 pathogenesis. Science. 2003;300(5618):486-9. doi: 10.1126/science.1079469. PubMed
820 PMID: 12702875.
821 27. Kayed R, Head E, Sarsoza F, Saing T, Cotman CW, Necula M, Margol L, Wu J, Breydo L,
822 Thompson JL, Rasool S, Gurlo T, Butler P, Glabe CG. Fibril specific, conformation
823 dependent antibodies recognize a generic epitope common to amyloid fibrils and fibrillar
824 oligomers that is absent in prefibrillar oligomers. Mol Neurodegener. 2007;2:18. Epub
825 20070926. doi: 10.1186/1750-1326-2-18. PubMed PMID: 17897471; PMCID:
826 PMC2100048.
827 28. Heiser V, Scherzinger E, Boeddrich A, Nordhoff E, Lurz R, Schugardt N, Lehrach H,
828 Wanker EE. Inhibition of huntingtin fibrillogenesis by specific antibodies and small
829 molecules: implications for Huntington's disease therapy. Proc Natl Acad Sci U S A.
830 2000;97(12):6739-44. doi: 10.1073/pnas.110138997. PubMed PMID: 10829068; PMCID:
831 PMC18723.
832 29. Sanchez I, Mahlke C, Yuan J. Pivotal role of oligomerization in expanded polyglutamine
833 neurodegenerative disorders. Nature. 2003;421(6921):373-9. doi: 10.1038/nature01301.
834 PubMed PMID: 12540902.
835 30. Tang Z, Su KH, Xu M, Dai C. HSF1 physically neutralizes amyloid oligomers to empower
836 overgrowth and bestow neuroprotection. Sci Adv. 2020;6(46). Epub 20201111. doi:
837 10.1126/sciadv.abc6871. PubMed PMID: 33177089; PMCID: PMC7673739.
838 31. Christensen JH, Nielsen MN, Hansen J, Fuchtbauer A, Fuchtbauer EM, West M, Corydon
839 TJ, Gregersen N, Bross P. Inactivation of the hereditary spastic paraplegia-associated Hspd1
840 gene encoding the Hsp60 chaperone results in early embryonic lethality in mice. Cell Stress
841 Chaperones. 2010;15(6):851-63. doi: 10.1007/s12192-010-0194-x. PubMed PMID:

842 20393889; PMCID: PMC3024079.
843 32. Fan F, Duan Y, Yang F, Trexler C, Wang H, Huang L, Li Y, Tang H, Wang G, Fang X, Liu
844 J, Jia N, Chen J, Ouyang K. Deletion of heat shock protein 60 in adult mouse cardiomyocytes
845 perturbs mitochondrial protein homeostasis and causes heart failure. Cell Death Differ.
846 2020;27(2):587-600. Epub 20190617. doi: 10.1038/s41418-019-0374-x. PubMed PMID:
847 31209364; PMCID: PMC7205885.
848 33. Su KH, Cao J, Tang Z, Dai S, He Y, Sampson SB, Benjamin IJ, Dai C. HSF1 critically
849 attunes proteotoxic stress sensing by mTORC1 to combat stress and promote growth. Nat
850 Cell Biol. 2016;18(5):527-39. Epub 20160404. doi: 10.1038/ncb3335. PubMed PMID:
851 27043084; PMCID: PMC5341796.
852 34. Johnson GL, Nakamura K. The c-jun kinase/stress-activated pathway: regulation, function
853 and role in human disease. Biochim Biophys Acta. 2007;1773(8):1341-8. Epub 20070104.
854 doi: 10.1016/j.bbamcr.2006.12.009. PubMed PMID: 17306896; PMCID: PMC1995559.
855 35. Battaglioni S, Benjamin D, Walchli M, Maier T, Hall MN. mTOR substrate phosphorylation
856 in growth control. Cell. 2022;185(11):1814-36. Epub 20220516. doi:
857 10.1016/j.cell.2022.04.013. PubMed PMID: 35580586.
858 36. Kim DH, Sarbassov DD, Ali SM, King JE, Latek RR, Erdjument-Bromage H, Tempst P,
859 Sabatini DM. mTOR interacts with raptor to form a nutrient-sensitive complex that signals to
860 the cell growth machinery. Cell. 2002;110(2):163-75. doi: 10.1016/s0092-8674(02)00808-5.
861 PubMed PMID: 12150925.
862 37. Schmidt EK, Clavarino G, Ceppi M, Pierre P. SUnSET, a nonradioactive method to monitor
863 protein synthesis. Nat Methods. 2009;6(4):275-7. Epub 20090322. doi: 10.1038/nmeth.1314.
864 PubMed PMID: 19305406.

865 38. Zhang T, Inesta-Vaquera F, Niepel M, Zhang J, Ficarro SB, Machleidt T, Xie T, Marto JA,
866 Kim N, Sim T, Laughlin JD, Park H, LoGrasso PV, Patricelli M, Nomanbhoy TK, Sorger
867 PK, Alessi DR, Gray NS. Discovery of potent and selective covalent inhibitors of JNK.
868 Chem Biol. 2012;19(1):140-54. doi: 10.1016/j.chembiol.2011.11.010. PubMed PMID:
869 22284361; PMCID: PMC3270411.
870 39. Moerke NJ, Aktas H, Chen H, Cantel S, Reibarkh MY, Fahmy A, Gross JD, Degterev A,
871 Yuan J, Chorev M, Halperin JA, Wagner G. Small-molecule inhibition of the interaction
872 between the translation initiation factors eIF4E and eIF4G. Cell. 2007;128(2):257-67. doi:
873 10.1016/j.cell.2006.11.046. PubMed PMID: 17254965.
874 40. Tolcher A, Goldman J, Patnaik A, Papadopoulos KP, Westwood P, Kelly CS, Bumgardner
875 W, Sams L, Geeganage S, Wang T, Capen AR, Huang J, Joseph S, Miller J, Benhadji KA,
876 Brail LH, Rosen LS. A phase I trial of LY2584702 tosylate, a p70 S6 kinase inhibitor, in
877 patients with advanced solid tumours. Eur J Cancer. 2014;50(5):867-75. Epub 20140115.
878 doi: 10.1016/j.ejca.2013.11.039. PubMed PMID: 24440085.
879 41. Porter AG, Janicke RU. Emerging roles of caspase-3 in apoptosis. Cell Death Differ.
880 1999;6(2):99-104. doi: 10.1038/sj.cdd.4400476. PubMed PMID: 10200555.
881 42. Boulares AH, Yakovlev AG, Ivanova V, Stoica BA, Wang G, Iyer S, Smulson M. Role of
882 poly(ADP-ribose) polymerase (PARP) cleavage in apoptosis. Caspase 3-resistant PARP
883 mutant increases rates of apoptosis in transfected cells. J Biol Chem. 1999;274(33):22932-40.
884 doi: 10.1074/jbc.274.33.22932. PubMed PMID: 10438458.
885 43. Huang J, Manning BD. The TSC1-TSC2 complex: a molecular switchboard controlling cell
886 growth. Biochem J. 2008;412(2):179-90. doi: 10.1042/BJ20080281. PubMed PMID:
887 18466115; PMCID: PMC2735030.

888 44. Dong B, Jaeger AM, Hughes PF, Loiselle DR, Hauck JS, Fu Y, Haystead TA, Huang J,
889 Thiele DJ. Targeting therapy-resistant prostate cancer via a direct inhibitor of the human heat
890 shock transcription factor 1. Sci Transl Med. 2020;12(574). doi:
891 10.1126/scitranslmed.abb5647. PubMed PMID: 33328331; PMCID: PMC10571035.
892 45. Sengupta S, Giaime E, Narayan S, Hahm S, Howell J, O'Neill D, Vlasuk GP, Saiah E.
893 Discovery of NV-5138, the first selective Brain mTORC1 activator. Sci Rep.
894 2019;9(1):4107. Epub 20190311. doi: 10.1038/s41598-019-40693-5. PubMed PMID:
895 30858438; PMCID: PMC6412019.
896 46. Kato T, Pothula S, Liu RJ, Duman CH, Terwilliger R, Vlasuk GP, Saiah E, Hahm S, Duman
897 RS. Sestrin modulator NV-5138 produces rapid antidepressant effects via direct mTORC1
898 activation. J Clin Invest. 2019;129(6):2542-54. Epub 20190416. doi: 10.1172/JCI126859.
899 PubMed PMID: 30990795; PMCID: PMC6546461.
900 47. Wolfson RL, Chantranupong L, Saxton RA, Shen K, Scaria SM, Cantor JR, Sabatini DM.
901 Sestrin2 is a leucine sensor for the mTORC1 pathway. Science. 2016;351(6268):43-8. Epub
902 20151008. doi: 10.1126/science.aab2674. PubMed PMID: 26449471; PMCID:
903 PMC4698017.
904 48. Yoon YJ, Kim JA, Shin KD, Shin DS, Han YM, Lee YJ, Lee JS, Kwon BM, Han DC.
905 KRIBB11 inhibits HSP70 synthesis through inhibition of heat shock factor 1 function by
906 impairing the recruitment of positive transcription elongation factor b to the hsp70 promoter.
907 J Biol Chem. 2011;286(3):1737-47. Epub 20101115. doi: 10.1074/jbc.M110.179440.
908 PubMed PMID: 21078672; PMCID: PMC3023468.
909 49. Caserta TM, Smith AN, Gultice AD, Reedy MA, Brown TL. Q-VD-OPh, a broad spectrum
910 caspase inhibitor with potent antiapoptotic properties. Apoptosis. 2003;8(4):345-52. doi:

911 10.1023/a:1024116916932. PubMed PMID: 12815277.
912 50. Chauvier D, Ankri S, Charriaut-Marlangue C, Casimir R, Jacotot E. Broad-spectrum caspase
913 inhibitors: from myth to reality? Cell Death Differ. 2007;14(2):387-91. Epub 20060929. doi:
914 10.1038/sj.cdd.4402044. PubMed PMID: 17008913.
915 51. Miao EA, Rajan JV, Aderem A. Caspase-1-induced pyroptotic cell death. Immunol Rev.
916 2011;243(1):206-14. doi: 10.1111/j.1600-065X.2011.01044.x. PubMed PMID: 21884178;
917 PMCID: PMC3609431.
918 52. Shan B, Pan H, Najafov A, Yuan J. Necroptosis in development and diseases. Genes Dev.
919 2018;32(5-6):327-40. doi: 10.1101/gad.312561.118. PubMed PMID: 29593066; PMCID:
920 PMC5900707.
921 53. Chen X, Comish PB, Tang D, Kang R. Characteristics and Biomarkers of Ferroptosis. Front
922 Cell Dev Biol. 2021;9:637162. Epub 20210121. doi: 10.3389/fcell.2021.637162. PubMed
923 PMID: 33553189; PMCID: PMC7859349.
924 54. Stockwell BR. Ferroptosis turns 10: Emerging mechanisms, physiological functions, and
925 therapeutic applications. Cell. 2022;185(14):2401-21. doi: 10.1016/j.cell.2022.06.003.
926 PubMed PMID: 35803244; PMCID: PMC9273022.
927 55. Yoshii SR, Mizushima N. Monitoring and Measuring Autophagy. Int J Mol Sci. 2017;18(9).
928 Epub 20170828. doi: 10.3390/ijms18091865. PubMed PMID: 28846632; PMCID:
929 PMC5618514.
930 56. Blommaart EF, Krause U, Schellens JP, Vreeling-Sindelarova H, Meijer AJ. The
931 phosphatidylinositol 3-kinase inhibitors wortmannin and LY294002 inhibit autophagy in
932 isolated rat hepatocytes. Eur J Biochem. 1997;243(1-2):240-6. doi: 10.1111/j.1432-
933 1033.1997.0240a.x. PubMed PMID: 9030745.

934 57. Schubert U, Anton LC, Gibbs J, Norbury CC, Yewdell JW, Bennink JR. Rapid degradation
935 of a large fraction of newly synthesized proteins by proteasomes. Nature.
936 2000;404(6779):770-4. doi: 10.1038/35008096. PubMed PMID: 10783891.
937 58. Kim LC, Cook RS, Chen J. mTORC1 and mTORC2 in cancer and the tumor
938 microenvironment. Oncogene. 2017;36(16):2191-201. Epub 20161017. doi:
939 10.1038/onc.2016.363. PubMed PMID: 27748764; PMCID: PMC5393956.
940 59. Zou Z, Tao T, Li H, Zhu X. mTOR signaling pathway and mTOR inhibitors in cancer:
941 progress and challenges. Cell Biosci. 2020;10:31. Epub 20200310. doi: 10.1186/s13578-020-
942 00396-1. PubMed PMID: 32175074; PMCID: PMC7063815.
943 60. Goloudina AR, Demidov ON, Garrido C. Inhibition of HSP70: a challenging anti-cancer
944 strategy. Cancer Lett. 2012;325(2):117-24. Epub 20120628. doi:
945 10.1016/j.canlet.2012.06.003. PubMed PMID: 22750096.
946 61. Jhaveri K, Taldone T, Modi S, Chiosis G. Advances in the clinical development of heat
947 shock protein 90 (Hsp90) inhibitors in cancers. Biochim Biophys Acta. 2012;1823(3):742-
948 55. Epub 20111029. doi: 10.1016/j.bbamcr.2011.10.008. PubMed PMID: 22062686;
949 PMCID: PMC3288123.
950 62. Pasqua AE, Sharp SY, Chessum NEA, Hayes A, Pellegrino L, Tucker MJ, Miah A, Wilding
951 B, Evans LE, Rye CS, Mok NY, Liu M, Henley AT, Gowan S, De Billy E, Te Poele R,
952 Powers M, Eccles SA, Clarke PA, Raynaud FI, Workman P, Jones K, Cheeseman MD. HSF1
953 Pathway Inhibitor Clinical Candidate (CCT361814/NXP800) Developed from a Phenotypic
954 Screen as a Potential Treatment for Refractory Ovarian Cancer and Other Malignancies. J
955 Med Chem. 2023;66(8):5907-36. Epub 20230405. doi: 10.1021/acs.jmedchem.3c00156.
956 PubMed PMID: 37017629; PMCID: PMC10150365.

957 63. Ali ES, Mitra K, Akter S, Ramproshad S, Mondal B, Khan IN, Islam MT, Sharifi-Rad J,
958 Calina D, Cho WC. Recent advances and limitations of mTOR inhibitors in the treatment of
959 cancer. Cancer Cell Int. 2022;22(1):284. Epub 20220915. doi: 10.1186/s12935-022-02706-8.
960 PubMed PMID: 36109789; PMCID: PMC9476305.
961 64. Wood KC, Gutkind JS. Challenges and Emerging Opportunities for Targeting mTOR in
962 Cancer. Cancer Res. 2022;82(21):3884-7. doi: 10.1158/0008-5472.CAN-22-0602. PubMed
963 PMID: 36321262; PMCID: PMC9634680.
964 65. Thomson AW, Turnquist HR, Raimondi G. Immunoregulatory functions of mTOR
965 inhibition. Nat Rev Immunol. 2009;9(5):324-37. doi: 10.1038/nri2546. PubMed PMID:
966 19390566; PMCID: PMC2847476.
967
968
969
970
971
972
973
974
975
976
977
978
979

Figure 1

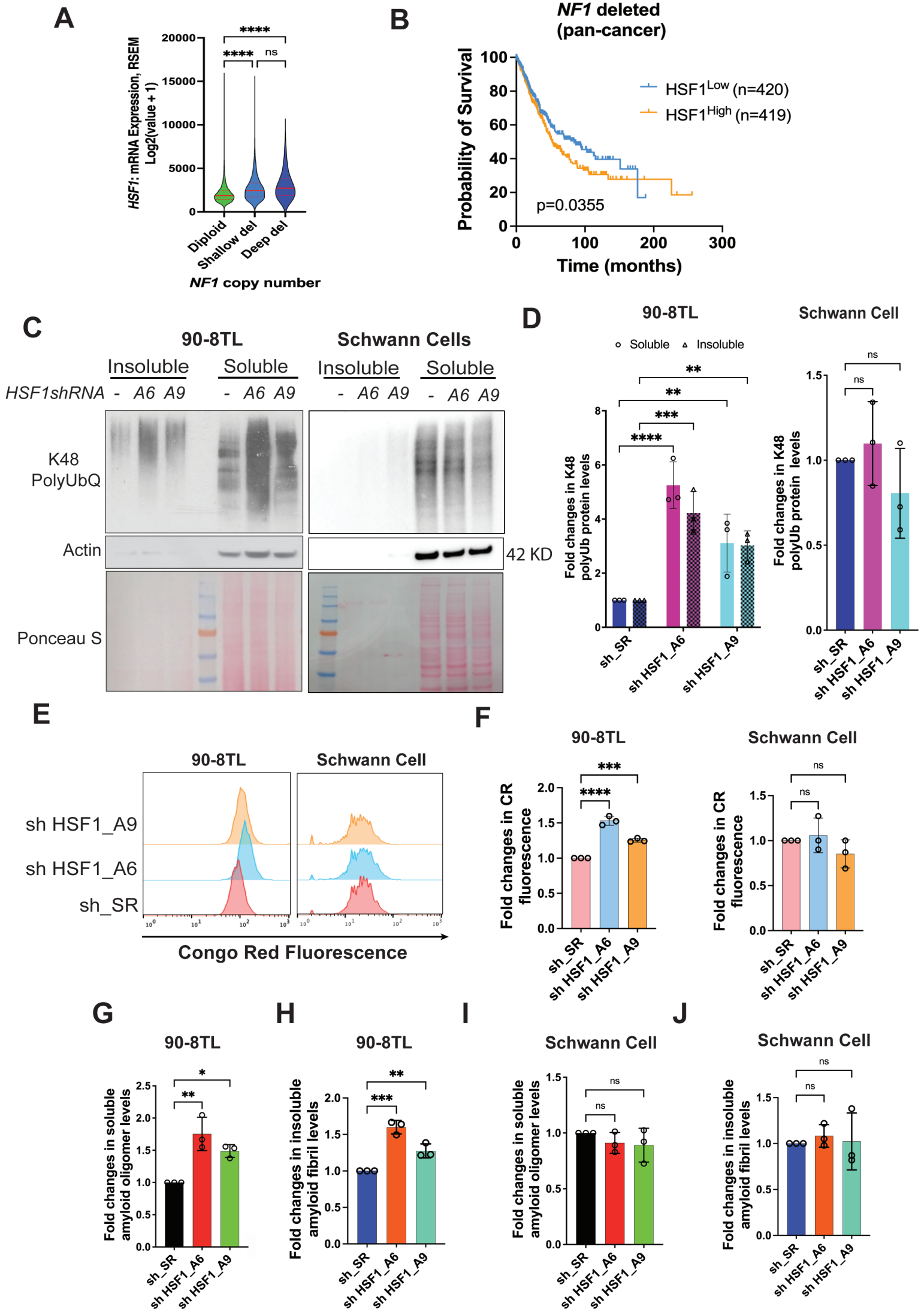
A
HSF1: mRNA Expression, RSEM Log2(value + 1)
20000
15000
10000
5000
0
****
****
ns
Diploid
Shallow del
Deep del
NF1 copy number
B
NF1 deleted (pan-cancer)
Probability of Survival
100
80
60
40
20
0
HSF1Low (n=420)
HSF1High (n=419)
p=0.0355
0
100
200
300
Time (months)
C
90-8TL
Schwann Cells
Insoluble
Soluble
Insoluble
Soluble
HSF1shRNA - A6 A9 - A6 A9 - A6 A9 - A6 A9
K48 PolyUbQ
Actin
42 KD
Ponceau S
D
90-8TL
Schwann Cell
Soluble
Insoluble
Fold changes in K48 polyUb protein levels
**
**
***
****
ns
ns
sh_SR
sh HSF1_A6
sh HSF1_A9
E
90-8TL
Schwann Cell
sh HSF1_A9
sh HSF1_A6
sh_SR
Congo Red Fluorescence
F
90-8TL
Schwann Cell
Fold changes in CR fluorescence
***
****
ns
ns
sh_SR
sh HSF1_A6
sh HSF1_A9
G
90-8TL
Fold changes in soluble amyloid oligomer levels
*
**
H
90-8TL
Fold changes in insoluble amyloid fibril levels
**
***
I
Schwann Cell
Fold changes in soluble amyloid oligomer levels
ns
ns
J
Schwann Cell
Fold changes in insoluble amyloid fibril levels
ns
ns

980 **FIGURE LEGENDS:**

981 **Figure 1: HSF1 is required to suppress proteomic instability and amyloidogenesis in**
982 **MPNST cells.** (A) Violin plots of *HSF1* expression in human cancer tissues showing *NF1*
983 deletion (median and IQR, n=6424, 1598, or 88, Kruskal-Wallis test). Data are generated by the
984 TGCA Research Network (https://www.cancer.gov/tcga). (B) Kaplan-Meier survival curves of
985 patients whose tumors harbor *NF1* deletion (n=420 or 419, Log-rank test). Data are generated by
986 the TGCA Research Network (https://www.cancer.gov/tcga). (C) and (D) The impacts of *HSF1*
987 depletion on protein polyubiquitination in both 90-8TL cells and primary human Schwann cells.
988 Cells were transduced with lentiviral shRNAs for 4 days and global protein Lys48-specific
989 ubiquitination was detected by immunoblotting in both detergent-soluble and -insoluble fractions
990 of whole cell lysates (C). Protein ubiquitination was quantitated using Fiji imaging software (D)
991 (mean ± SD, n=3 independent experiments, Two-way ANOVA). (E) and (F) Congo Red (CR)
992 staining of 90-8TL cells and primary human Schwann cells with and without *HSF1* depletion,
993 analyzed by flow cytometry (E). Quantitation of CR staining using the median fluorescence
994 intensity (F) (mean ± SD, n=3 independent experiments, One-way ANOVA). (G)-(J)
995 Quantitation of soluble amyloid oligomers and insoluble amyloid fibrils by ELISA using A11
996 and OC antibodies, respectively (mean ± SD, n=3 independent experiments, One-way ANOVA).
997
998
999
1000
1001
1002

Figure 2

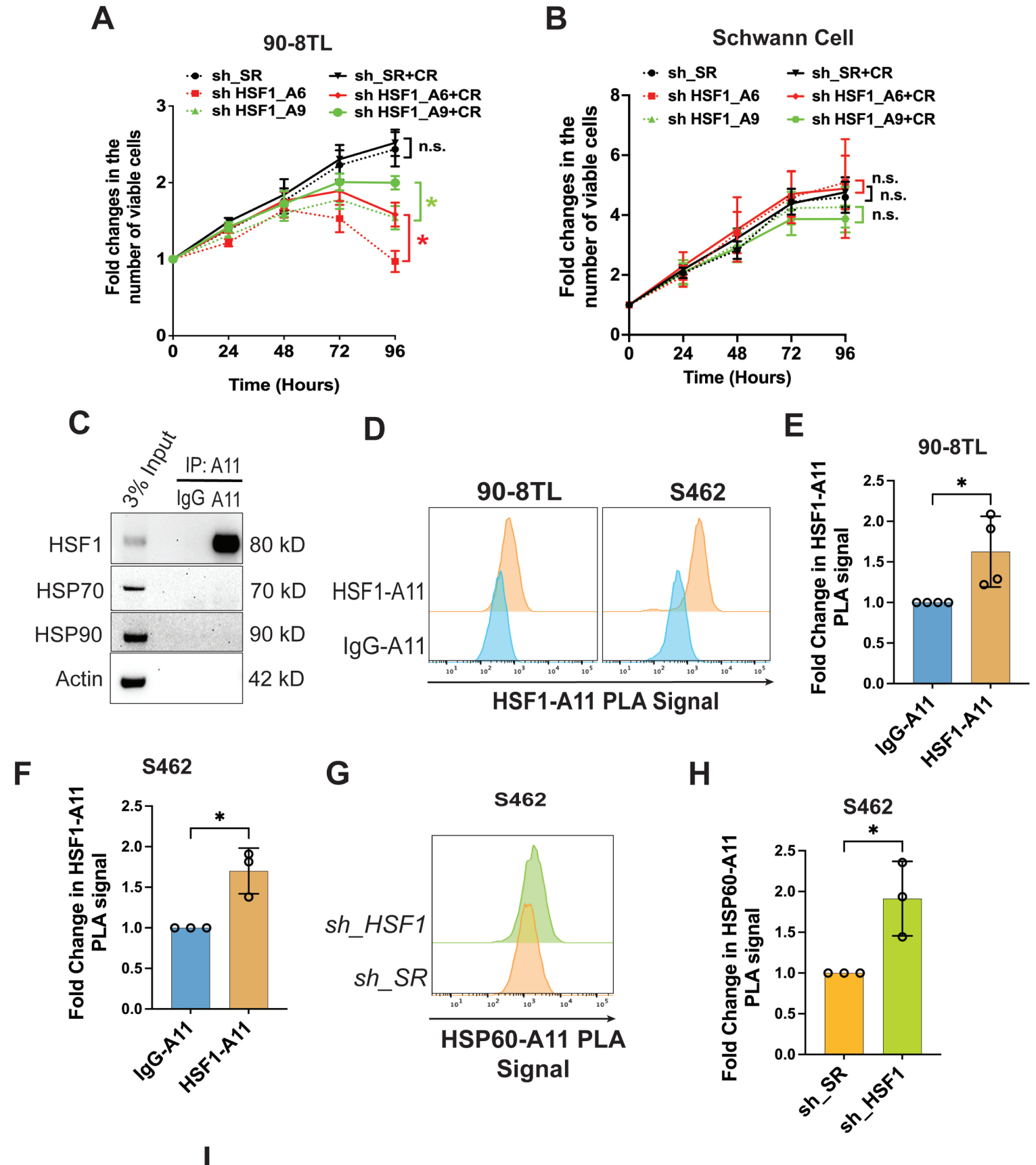
A
90-8TL
sh_SR
sh HSF1_A6
sh HSF1_A9
sh_SR+CR
sh HSF1_A6+CR
sh HSF1_A9+CR
Fold changes in the number of viable cells
Time (Hours)
n.s.
*
*
B
Schwann Cell
sh_SR
sh HSF1_A6
sh HSF1_A9
sh_SR+CR
sh HSF1_A6+CR
sh HSF1_A9+CR
Fold changes in the number of viable cells
Time (Hours)
n.s.
n.s.
n.s.
C
3% Input
IP: A11
IgG A11
HSF1
HSP70
HSP90
Actin
80 kD
70 kD
90 kD
42 kD
D
90-8TL
S462
HSF1-A11
IgG-A11
HSF1-A11 PLA Signal
E
90-8TL
Fold Change in HSF1-A11 PLA signal
*
IgG-A11
HSF1-A11
F
S462
Fold Change in HSF1-A11 PLA signal
*
IgG-A11
HSF1-A11
G
S462
sh_HSF1
sh_SR
HSP60-A11 PLA Signal
H
S462
Fold Change in HSP60-A11 PLA signal
*
sh_SR
sh_HSF1
I
Mitochondrial proteomic stability
Mitochondrial proteomic instability
HSF1
HSP60
AO

1003 **Figure 2: HSF1 counters the tumor-suppressive effects of amyloids in MPNST cells.**
1004 (A) and (B) The growth curves of 90-8TL and primary human Schwann cells with and without
1005 *HSF1* depletion and 20 μM CR treatment (mean ± SD, n=3 independent experiments, Two-way
1006 ANOVA). (C) Co-IP of amyloid oligomers (AOs) with HSF1 in 90-8TL cells. (D)-(F) Detection
1007 of AO–HSF1 interactions by PLA flow cytometry in 90-8TL and S462 cells. Quantitation of the
1008 PLA signals using the median fluorescence intensity (mean ± SD, n=3 or 4 independent
1009 experiments, Student's t test). (G) and (H) Detection of AO–HSP60 interactions by PLA flow
1010 cytometry in S462 cells following *HSF1* depletion (G). Quantitation of the PLA signals using the
1011 median fluorescence intensity (H) (mean ± SD, n=3 independent experiments, Student's t test).
1012 (I) Schematic depiction of AO neuralization by HSF1 and HSP60 attack by AO following *HSF1*
1013 depletion in mitochondria.
1014
1015
1016
1017
1018
1019
1020
1021
1022
1023
1024
1025

Figure 3

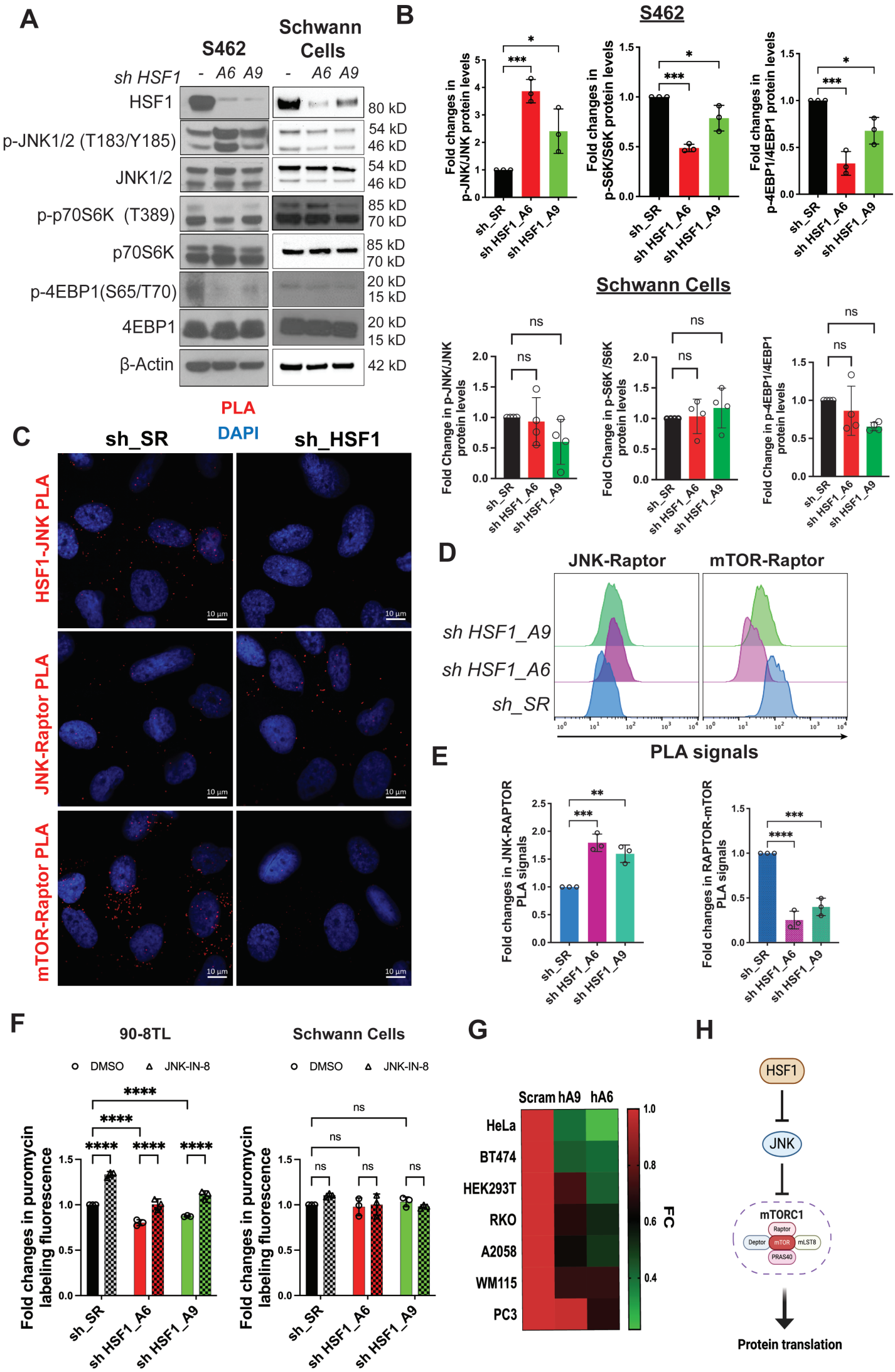
A
S462
Schwann Cells
sh HSF1
- A6 A9
- A6 A9
HSF1
p-JNK1/2 (T183/Y185)
JNK1/2
p-p70S6K (T389)
p70S6K
p-4EBP1(S65/T70)
4EBP1
β-Actin
80 kD
54 kD
46 kD
54 kD
46 kD
85 kD
70 kD
85 kD
70 kD
20 kD
15 kD
20 kD
15 kD
42 kD
B
S462
Fold changes in p-JNK/JNK protein levels
Fold changes in p-S6K/S6K protein levels
Fold changes in p-4EBP1/4EBP1 protein levels
sh_SR
sh HSF1_A6
sh HSF1_A9
Schwann Cells
Fold Change in p-JNK/JNK protein levels
Fold Change in p-S6K /S6K protein levels
Fold Change in p-4EBP1/4EBP1 protein levels
ns
C
PLA
DAPI
sh_SR
sh_HSF1
HSF1-JNK PLA
JNK-Raptor PLA
mTOR-Raptor PLA
10 µm
D
JNK-Raptor
mTOR-Raptor
sh HSF1_A9
sh HSF1_A6
sh_SR
PLA signals
E
Fold changes in JNK-RAPTOR PLA signals
Fold changes in RAPTOR-mTOR PLA signals
sh_SR
sh HSF1_A6
sh HSF1_A9
F
90-8TL
Schwann Cells
DMSO
JNK-IN-8
Fold changes in puromycin labeling fluorescence
sh_SR
sh HSF1_A6
sh HSF1_A9
G
Scram hA9 hA6
HeLa
BT474
HEK293T
RKO
A2058
WM115
PC3
FC
H
HSF1
JNK
mTORC1
Raptor
Deptor
mTOR
mLST8
PRAS40
Protein translation

1026 **Figure 3: JNK senses *HSF1* deficiency to repress mTORC1 and protein translation in**
1027 **MPNST cells.** (A) Detection of JNK activation and mTORC1 inhibition following *HSF1*
1028 depletion in S462 and primary human Schwann cells by immunoblotting. (B) Quantitation of (A)
1029 using Fiji imaging software (mean ± SD, n=3 independent experiments, One-way ANOVA). (C)
1030 Detection of HSF1-JNK, JNK-RAPTOR, and mTOR-RAPTOR interactions by PLA in S462
1031 cells with and without *HSF1* depletion. (D) and (E) Detection and quantitation of JNK-RAPTOR
1032 and mTOR-RAPTOR interactions by PLA flow cytometry in 90-8TL cells (mean ± SD, n=3
1033 independent experiments, One-way ANOVA). (F) Measurement of protein translation rates in
1034 90-8TL and primary human Schwann cells with and without *HSF1* depletion by puromycin
1035 labeling, analyzed by flow cytometry. Cells were treated with 1 μM JNK-IN-8 for 24 hrs before
1036 labeling with 100 nM 6-FAM-dc-puromycin for 30 min (mean ± SD, n=3 independent
1037 experiments, Two-way ANOVA). (G) Heatmap of protein translation rates measured by
1038 puromycin labeling in diverse human cancer cell lines with and without *HSF1* depletion. (H)
1039 Schematic depiction of regulation of protein translation by HSF1.
1040
1041
1042
1043
1044
1045
1046
1047
1048

Figure 4

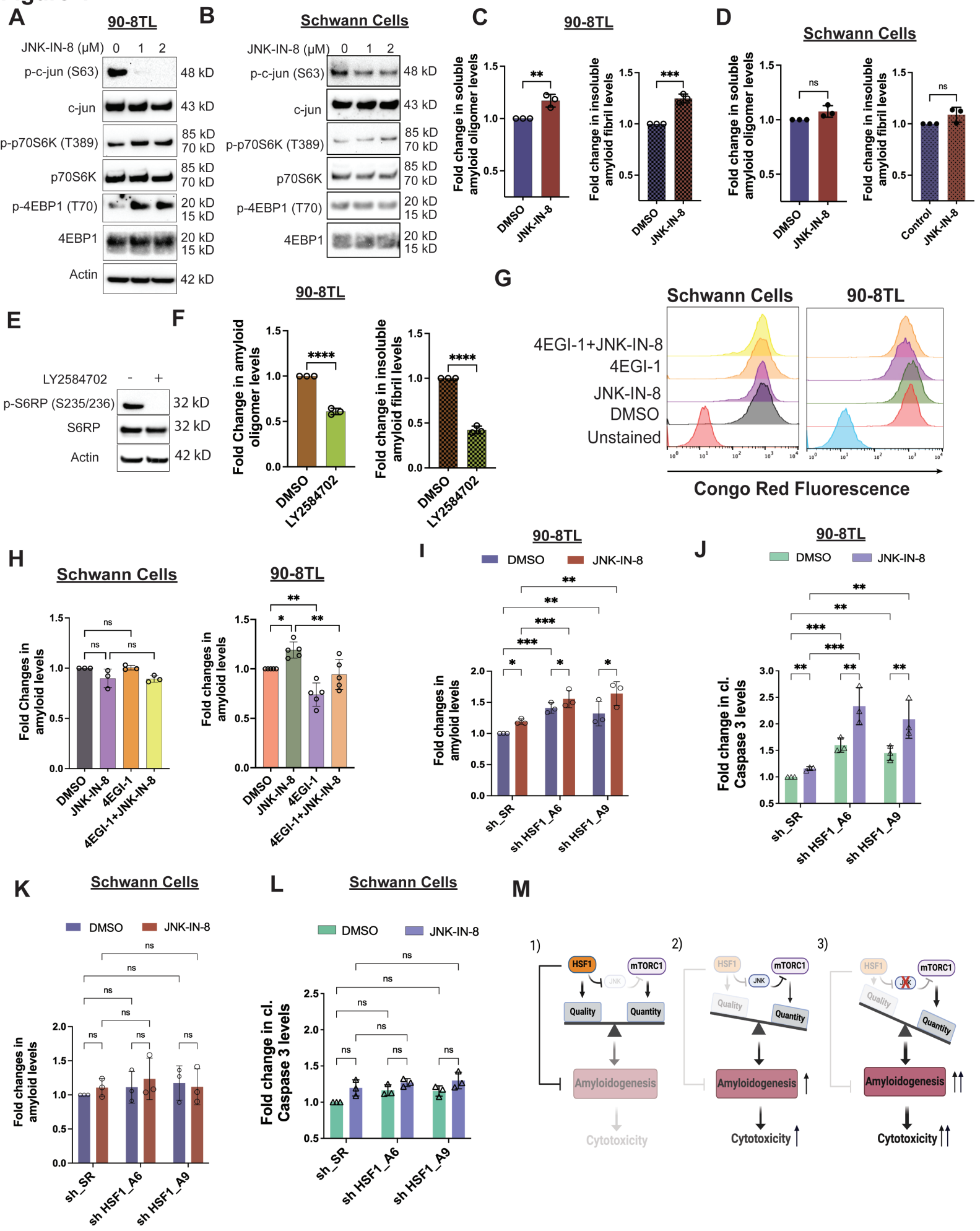
A
90-8TL
JNK-IN-8 (μM) 0 1 2
p-c-jun (S63) 48 kD
c-jun 43 kD
p-p70S6K (T389) 85 kD 70 kD
p70S6K 85 kD 70 kD
p-4EBP1 (T70) 20 kD 15 kD
4EBP1 20 kD 15 kD
Actin 42 kD
B
Schwann Cells
JNK-IN-8 (μM) 0 1 2
p-c-jun (S63) 48 kD
c-jun 43 kD
p-p70S6K (T389) 85 kD 70 kD
p70S6K 85 kD 70 kD
p-4EBP1 (T70) 20 kD 15 kD
4EBP1 20 kD 15 kD
C
90-8TL
Fold change in soluble amyloid oligomer levels
Fold change in insoluble amyloid fibril levels
DMSO
JNK-IN-8
D
Schwann Cells
Fold change in soluble amyloid oligomer levels
Fold change in insoluble amyloid fibril levels
ns
DMSO
JNK-IN-8
Control
E
LY2584702 - +
p-S6RP (S235/236) 32 kD
S6RP 32 kD
Actin 42 kD
F
90-8TL
Fold Change in amyloid oligomer levels
Fold change in insoluble amyloid fibril levels
DMSO
LY2584702
G
Schwann Cells
90-8TL
4EGI-1+JNK-IN-8
4EGI-1
JNK-IN-8
DMSO
Unstained
Congo Red Fluorescence
H
Schwann Cells
90-8TL
Fold Changes in amyloid levels
Fold changes in amyloid levels
DMSO
JNK-IN-8
4EGI-1
4EGI-1+JNK-IN-8
I
90-8TL
DMSO
JNK-IN-8
Fold changes in amyloid levels
sh_SR
sh HSF1_A6
sh HSF1_A9
J
90-8TL
DMSO
JNK-IN-8
Fold change in cl. Caspase 3 levels
sh_SR
sh HSF1_A6
sh HSF1_A9
K
Schwann Cells
DMSO
JNK-IN-8
Fold changes in amyloid levels
sh_SR
sh HSF1_A6
sh HSF1_A9
L
Schwann Cells
DMSO
JNK-IN-8
Fold change in cl. Caspase 3 levels
sh_SR
sh HSF1_A6
sh HSF1_A9
M
1)
2)
3)
HSF1
mTORC1
JNK
Quality
Quantity
Amyloidogenesis
Cytotoxicity

1049 **Figure 4: Protein translation is causally related to amyloidogenesis in MPNST cells.**
1050 (A) and (B) Detection of mTORC1 stimulation following JNK inhibition in 90-8TL and
1051 immortalized human Schwann cells by immunoblotting. Cells were treated with JNK-IN-8 for 2
1052 days. (C) and (D) Quantitation of soluble AOs and insoluble AFs by ELISA in 90-8TL and
1053 human Schwann cells with and without 3 μM JNK-IN-8 treatment for 3 days (mean ± SD, n=3
1054 independent experiments, Student's t test). (E) Detection of LY2584702-mediated S6K
1055 inhibition in 90-8TL cells by immunoblotting. Cells were treated with 20 μM LY2584702 for 2
1056 days. (F) Quantitation of soluble AOs and insoluble AFs by ELISA in 90-8TL cells with and
1057 without 20 μM LY2584702 treatment for 2 days (mean ± SD, n=3 independent experiments,
1058 Student's t test). (G) CR staining of 90-8TL and immortalized human Schwann cells with and
1059 without JNK-IN-8 and 4EGI-1 treatment, detected by flow cytometry. (H) Quantitation of (G)
1060 using the median fluorescence intensity (mean ± SD, n=3 independent experiments, One-way
1061 ANOVA). (I) Quantitation of amyloids by CR staining in 90-8TL cells with and without *HSF1*
1062 depletion and 3 μM JNK-IN-8 treatment (mean ± SD, n=3 independent experiments, Two-way
1063 ANOVA). (J) Quantitation of caspase 3 cleavage by ELISA in 90-8TL cells with and without
1064 *HSF1* depletion and 3 μM JNK-IN-8 treatment (mean ± SD, n=3 independent experiments, Two-
1065 way ANOVA). (K) Quantitation of amyloids by CR staining in immortalized human Schwann
1066 cells with and without *HSF1* depletion and 3 μM JNK-IN-8 treatment (mean ± SD, n=3
1067 independent experiments, Two-way ANOVA). (L) Quantitation of caspase 3 cleavage by ELISA
1068 in immortalized human Schwann cells with and without *HSF1* depletion and 3 μM JNK-IN-8
1069 treatment (mean ± SD, n=3 independent experiments, Two-way ANOVA). (M) Schematic
1070 depiction of the adaptation of MPNST cells to *HSF1* depletion by activating JNK to suppress
1071 mTORC1 and protein translation, thereby alleviating amyloidogenesis and cytotoxicity.

Figure 5

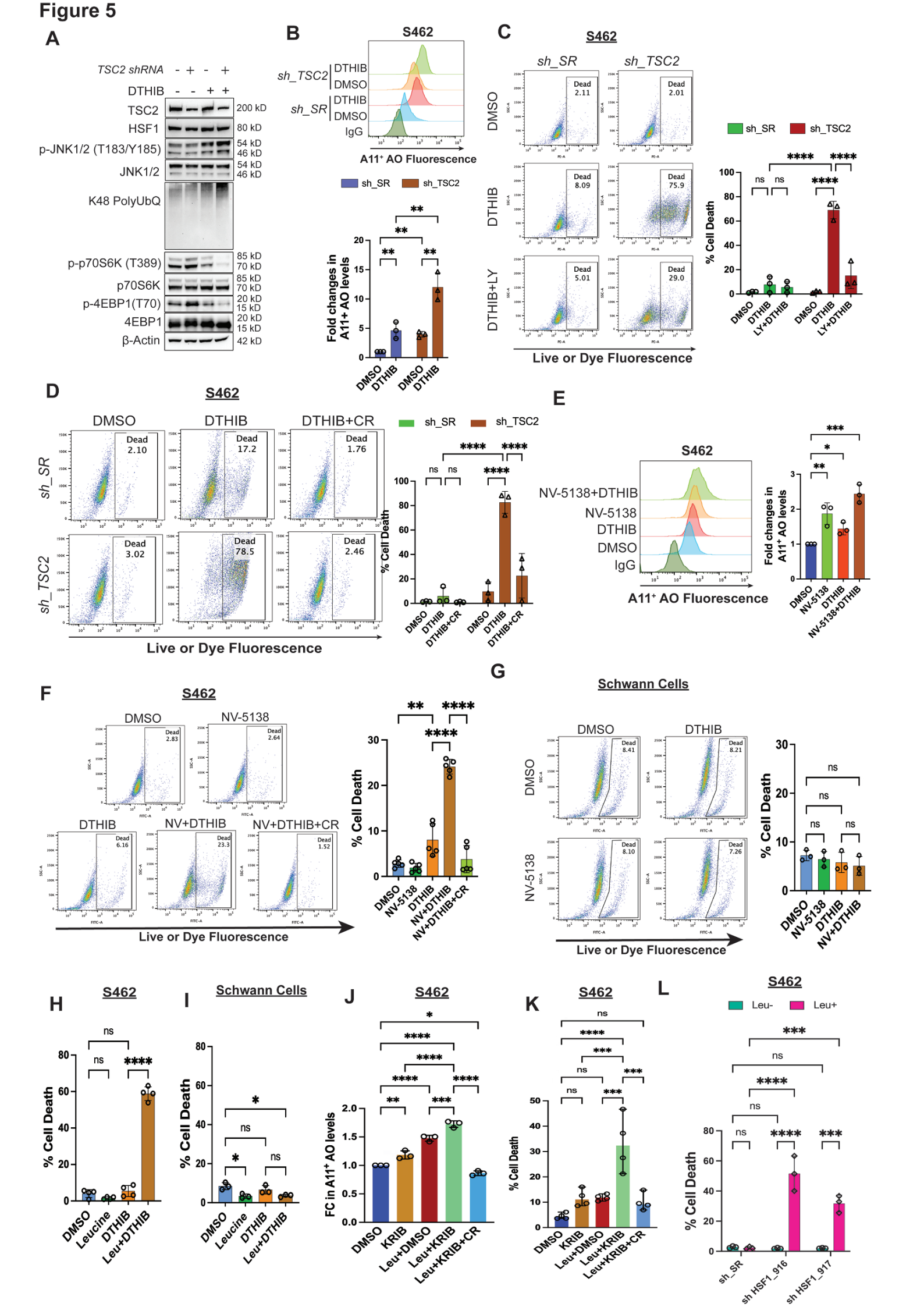
A
TSC2 shRNA - + - +
DTHIB - - + +
TSC2
HSF1
p-JNK1/2 (T183/Y185)
JNK1/2
K48 PolyUbQ
p-p70S6K (T389)
p70S6K
p-4EBP1(T70)
4EBP1
β-Actin
200 kD
80 kD
54 kD
46 kD
85 kD
70 kD
20 kD
15 kD
42 kD
B
S462
sh_TSC2
DTHIB
DMSO
sh_SR
IgG
A11+ AO Fluorescence
sh_SR
sh_TSC2
Fold changes in A11+ AO levels
DMSO
DTHIB
C
S462
sh_SR
sh_TSC2
DMSO
DTHIB
DTHIB+LY
Dead 2.11
Dead 2.01
Dead 8.09
Dead 75.9
Dead 5.01
Dead 29.0
Live or Dye Fluorescence
% Cell Death
LY+DTHIB
D
S462
DMSO
DTHIB
DTHIB+CR
sh_SR
sh_TSC2
Dead 2.10
Dead 17.2
Dead 1.76
Dead 3.02
Dead 78.5
Dead 2.46
Live or Dye Fluorescence
% Cell Death
E
S462
NV-5138+DTHIB
NV-5138
DTHIB
DMSO
IgG
A11+ AO Fluorescence
Fold changes in A11+ AO levels
F
S462
DMSO
NV-5138
DTHIB
NV+DTHIB
NV+DTHIB+CR
Dead 2.83
Dead 2.64
Dead 6.16
Dead 23.3
Dead 1.52
Live or Dye Fluorescence
% Cell Death
G
Schwann Cells
DMSO
DTHIB
NV-5138
Dead 8.41
Dead 8.21
Dead 8.10
Dead 7.26
Live or Dye Fluorescence
% Cell Death
H
S462
% Cell Death
DMSO
Leucine
DTHIB
Leu+DTHIB
I
Schwann Cells
% Cell Death
J
S462
FC in A11+ AO levels
DMSO
KRIB
Leu+DMSO
Leu+KRIB
Leu+KRIB+CR
K
S462
% Cell Death
L
S462
Leu-
Leu+
% Cell Death
sh_SR
sh HSF1_916
sh HSF1_917

1072 **Figure 5: mTORC1 stimulation aggravates the amyloidogenesis and cytotoxicity elicited by**
1073 **HSF1 inhibition.** (A) Immunoblotting detection of JNK activation, mTORC1 activity, and
1074 protein polyubiquitination in S462 cells following stable *TSC2* knockdown and/or HSF1
1075 inhibition by 10 μM DTHIB for 3 days. (B) Quantitation of soluble AOs by flow cytometry
1076 using A11 antibody staining in S462 cells with and without *TSC2* knockdown and 10 μM
1077 DTHIB treatment (mean ± SD, n=3 independent experiments, Two-way ANOVA). (C)
1078 Quantitation of cytotoxicity by flow cytometry using Live-or-Dye stains in S462 cells with and
1079 without stable *TSC2* knockdown and DTHIB (10 μM) or combined DTHIB and LY2584702 (20
1080 μM) treatment (mean ± SD, n=3 independent experiments, Two-way ANOVA). Cells were pre-
1081 treated with LY2584702 for 1 day followed by DTHIB treatment for another 3 days. (D)
1082 Quantitation of cytotoxicity by flow cytometry using Live-or-Dye stains in S462 cells with and
1083 without stable *TSC2* knockdown and DTHIB (10 μM) or combined DTHIB and CR (30 μM)
1084 treatment (mean ± SD, n=3 independent experiments, Two-way ANOVA). Cells were pre-
1085 treated with CR for 1 day followed by DTHIB treatment for another 3 days. (E) Quantitation of
1086 soluble AOs by flow cytometry using A11 antibody staining in S462 cells with and without 500
1087 μM NV-5138 stimulation and 10 μM DTHIB treatment (mean ± SD, n=3 independent
1088 experiments, One-way ANOVA). (F) Quantitation of cytotoxicity by flow cytometry using Live-
1089 or-Dye stains in S462 cells with and without 500 μM NV-5138 stimulation and 10 μM DTHIB
1090 or combined DTHIB and CR treatment (mean ± SD, n=5 independent experiments, One-way
1091 ANOVA). (G) Quantitation of cytotoxicity by flow cytometry using Live-or-Dye stains in
1092 immortalized human Schwann cells with and without 500 μM NV-5138 stimulation and 10 μM
1093 DTHIB treatment (mean ± SD, n=3 independent experiments, One-way ANOVA). (H)
1094 Quantitation of cytotoxicity by flow cytometry using Live-or-Dye stains in S462 cells with and

1095 without 500 μM L-leucine stimulation and 10 μM DTHIB treatment (mean ± SD, n=4
1096 independent experiments, One-way ANOVA). (I) Quantitation of cytotoxicity by flow cytometry
1097 using Live-or-Dye stains in immortalized human Schwann cells with and without 500 μM L-
1098 leucine stimulation and 10 μM DTHIB treatment (mean ± SD, n=3 independent experiments,
1099 One-way ANOVA). (J) Quantitation of soluble AOs by ELISA in S462 cells treated with and
1100 without 800 μM L-leucine and 20 μM KRIBB11 or 30 μM CR (mean ± SD, n=3 independent
1101 experiments, One-way ANOVA). (K) Quantitation of cytotoxicity by flow cytometry using Live-
1102 or-Dye stains in S462 cells treated as above (mean ± SD, n=4 independent experiments, One-
1103 way ANOVA). (L) Quantitation of cytotoxicity by flow cytometry using Live-or-Dye stains in
1104 S462 cells stably expressing inducible shRNAs with and without L-leucine stimulation. Cells
1105 were first cultured with or without 1.2 mM L-leucine for 2 days, followed by addition of 20
1106 ng/ml doxycycline for 7 days (mean ± SD, n=3 independent experiments, One-way ANOVA).
1107
1108
1109
1110
1111
1112
1113
1114
1115
1116
1117

Figure 6

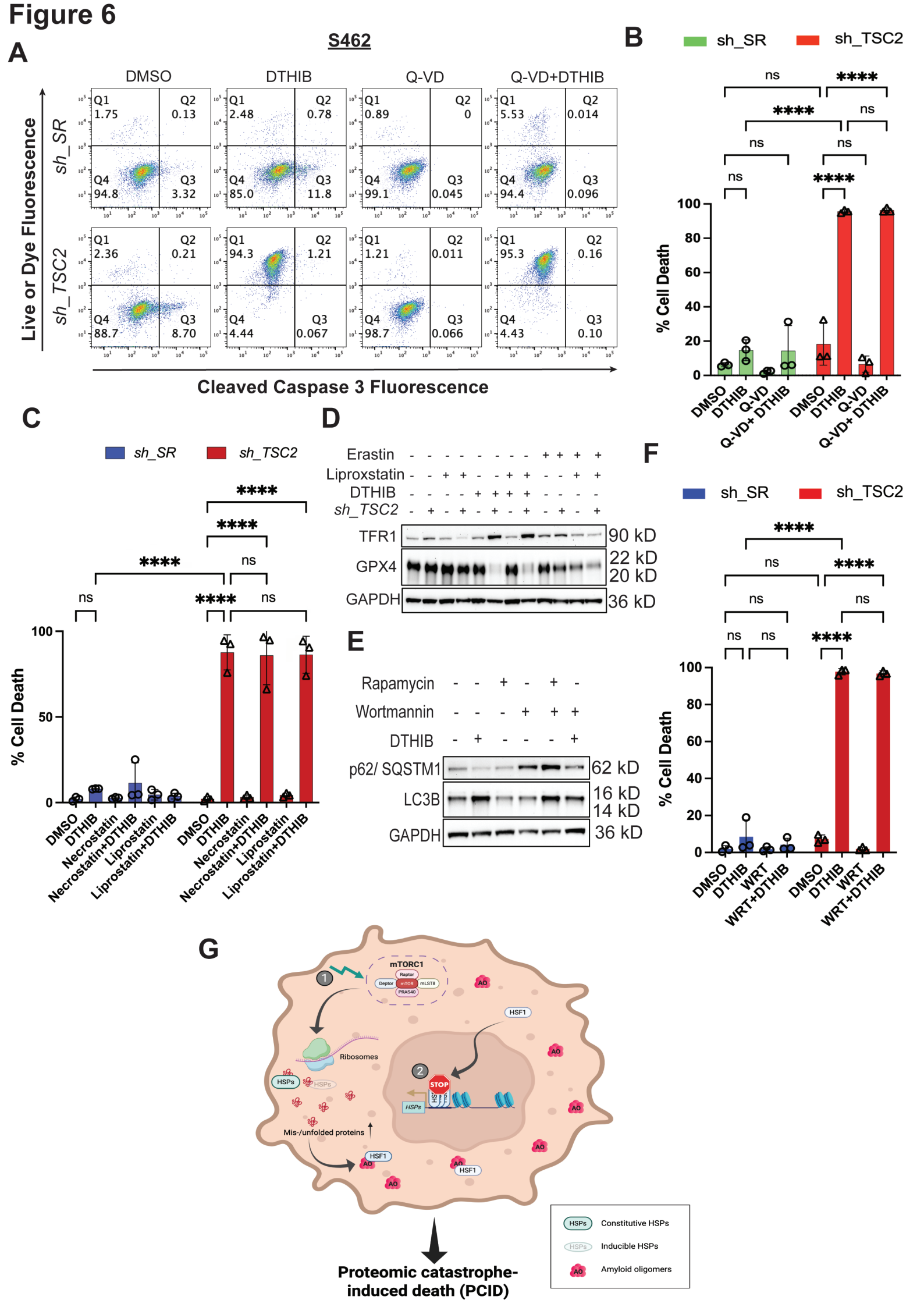
A
S462
DMSO
DTHIB
Q-VD
Q-VD+DTHIB
sh_SR
sh_TSC2
Q1 1.75
Q2 0.13
Q4 94.8
Q3 3.32
Q1 2.48
Q2 0.78
Q4 85.0
Q3 11.8
Q1 0.89
Q2 0
Q4 99.1
Q3 0.045
Q1 5.53
Q2 0.014
Q4 94.4
Q3 0.096
Q1 2.36
Q2 0.21
Q4 88.7
Q3 8.70
Q1 94.3
Q2 1.21
Q4 4.44
Q3 0.067
Q1 1.21
Q2 0.011
Q4 98.7
Q3 0.066
Q1 95.3
Q2 0.16
Q4 4.43
Q3 0.10
Live or Dye Fluorescence
Cleaved Caspase 3 Fluorescence
B
sh_SR
sh_TSC2
% Cell Death
DMSO
DTHIB
Q-VD
Q-VD+ DTHIB
C
sh_SR
sh_TSC2
% Cell Death
DMSO
DTHIB
Necrostatin
Necrostatin+DTHIB
Liprostatin
Liprostatin+DTHIB
D
Erastin
Liproxstatin
DTHIB
sh_TSC2
TFR1
GPX4
GAPDH
90 kD
22 kD
20 kD
36 kD
E
Rapamycin
Wortmannin
DTHIB
p62/ SQSTM1
LC3B
GAPDH
62 kD
16 kD
14 kD
36 kD
F
sh_SR
sh_TSC2
% Cell Death
DMSO
DTHIB
WRT
WRT+DTHIB
G
mTORC1
Raptor
Deptor
mTOR
mLST8
PRAS40
HSF1
Ribosomes
HSPs
STOP
HSPs
Mis-/unfolded proteins
Constitutive HSPs
Inducible HSPs
Amyloid oligomers
Proteomic catastrophe-induced death (PCID)

1118 **Figure 6: Concurrent HSF1 inhibition and mTORC1 stimulation instigate widespread non-**
1119 **apoptotic cell death.** (A) and (B) Quantitation of cytotoxicity by flow cytometry using Live-or-
1120 Dye stains combined with cleaved caspase 3 (Asp175) antibody staining. S462 cells with and
1121 without stable *TSC2* knockdown were treated with DMSO, 10 μM DTHIB, or combined DTHIB
1122 and 30 μM Q-VD-OPh (mean ± SD, n=3 independent experiments, Two-way ANOVA). (C)
1123 Quantitation of cytotoxicity by flow cytometry using Live-or-Dye stains in S462 cells with and
1124 without stable *TSC2* knockdown. Cells were treated with 10 μM DTHIB alone or co-treated with
1125 10 μM DTHIB and 30 μM Necrostatin-1 or 20 μM Liproxstatin-1 for 3 days (mean ± SD, n=3
1126 independent experiments, Two-way ANOVA). (D) Immunoblotting detection of ferroptosis
1127 markers in S462 cells with and without stable *TSC2* knockdown treated with 10 μM DTHIB
1128 alone or co-treated with 10 μM DTHIB and 20 μM liproxstatin-1 for 3 days. Erastin was
1129 included as a positive control to induce canonical ferroptosis. (E) Immunoblotting detection of
1130 autophagy markers in S462 cells with stable *TSC2* knockdown treated with 10 μM DTHIB alone
1131 or co-treated with 10 μM DTHIB and 3 μM wortmannin for 3 days. Rapamycin was included as
1132 a positive control to induce autophagy. (F) Quantitation of cytotoxicity by flow cytometry using
1133 Live-or-Dye stains in S462 cells with and without stable *TSC2* knockdown. Cells were treated
1134 with 10 μM DTHIB alone or co-treated with 10 μM DTHIB and 3 μM wortmannin for 3 days
1135 (mean ± SD, n=3 independent experiments, Two-way ANOVA). (G) Schematic depiction of
1136 instigation of cell death by severe proteomic imbalance, owing to simultaneous mTORC1
1137 stimulation (❶) and HSF1 inhibition (❷). In cancer cells, constitutive HSF1 activation
1138 provides extra chaperoning capacity to cope with elevated protein misfolding, partly due to
1139 enhanced protein synthesis and widespread genetic mutations. Nevertheless, amyloids still
1140 emerge, although at low levels. Importantly, HSF1 can neutralize highly toxic amyloid

oligomers, averting lethal consequences. By contrast, HSF1 inhibition diminishes chaperoning capacity, insufficient to counterbalance the robust protein translation. mTORC1 stimulation further aggravates this proteomic imbalance, which, in turn, promotes amyloidogenesis and proteomic catastrophe. In consequence, the amounts of amyloid oligomers surpass the neutralizing capacity of HSF1, leading to cell death; nonetheless, it remains unclear how this proteomic catastrophe-induced death (PCID) occurs.

Figure 7

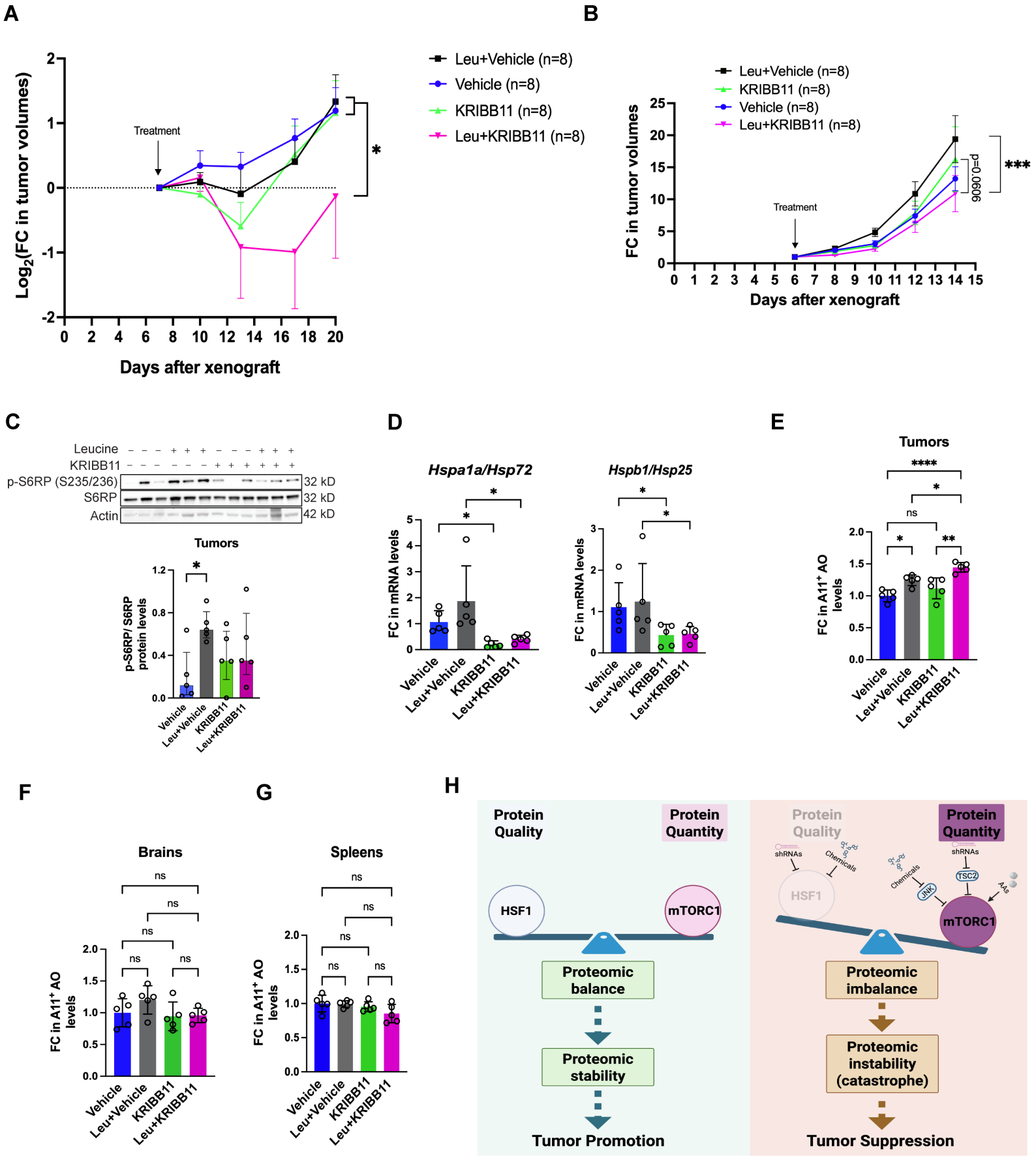
A
Log2(FC in tumor volumes)
Treatment
Days after xenograft
Leu+Vehicle (n=8)
Vehicle (n=8)
KRIBB11 (n=8)
Leu+KRIBB11 (n=8)
B
FC in tumor volumes
Treatment
Days after xenograft
p=0.0606
C
Leucine
KRIBB11
p-S6RP (S235/236)
S6RP
Actin
32 kD
32 kD
42 kD
Tumors
p-S6RP/ S6RP protein levels
Vehicle
Leu+Vehicle
KRIBB11
Leu+KRIBB11
D
Hspa1a/Hsp72
Hspb1/Hsp25
FC in mRNA levels
E
Tumors
FC in A11+ AO levels
F
Brains
G
Spleens
H
Protein Quality
Protein Quantity
HSF1
mTORC1
Proteomic balance
Proteomic stability
Tumor Promotion
shRNAs
Chemicals
JNK
TSC2
Akt
Proteomic imbalance
Proteomic instability (catastrophe)
Tumor Suppression

1164 **Figure 7: Concurrent HSF1 inhibition and mTORC1 stimulation suppress *in vivo* tumor**
1165 **growth.** (A) Combined KRIBB11 treatment and L-leucine stimulation impaired the *in vivo*
1166 growth of xenografted S462 human MPNST cells in NIH-III nude mice (mean ± SEM, n=8 mice
1167 per group, $\log_2$ transformation for Two-way ANOVA). (B) Combined KRIBB11 treatment and
1168 L-leucine stimulation impeded the *in vivo* growth of xenografted B16-F10 murine melanoma
1169 cells in C57BL/6J mice (mean ± SEM, n=8 mice per group, $\log_2$ transformation for Two-way
1170 ANOVA). (C) Quantitation of phospho-S6RP by immunoblotting in treated melanomas. Images
1171 show representative 3 tumors each group (mean ± SEM, n=5 tumors per group, One-way
1172 ANOVA). (D) Quantitation of *Hsp72* and *Hsp25* mRNAs in treated melanomas by RT-qPCR
1173 (mean ± SD, n=5 tumors per group, One-way ANOVA). (E) Quantitation of soluble AOs in
1174 treated B16F10 melanomas by ELISA ((mean ± SD, n=5 tumors per group, One-way ANOVA).
1175 (F) and (G) Quantitation of soluble AOs in brains and spleens from treated C57BL/6J mice by
1176 ELISA (mean ± SD, n=5 brains or spleens per group, One-way ANOVA). (H) Schematic
1177 depiction of the concept of provoking proteomic catastrophe to combat malignancy. On the one
1178 hand, in cancer cells, mTORC1 is inevitably activated to stimulate protein translation, markedly
1179 augmenting protein quantity. On the other hand, the extra chaperoning capacity governed by
1180 HSF1, albeit dispensable for normal life, becomes necessary to ensure sufficient protein quality
1181 in cancer cells, thereby counterbalancing augmented protein quantity and suppressing proteomic
1182 instability. Thus, proteomic balance promotes malignant growth. By contrast, disrupting
1183 proteomic balance, through HSF1 inhibition, is sufficient to elicit proteomic instability and
1184 tumor suppression. However, simultaneous mTORC1 stimulation can remarkably drive
1185 proteomic imbalance, causing proteomic catastrophe that leads to tumor suppression.